CHALMERS
UNIVERSITY OF TECHNOLOGY

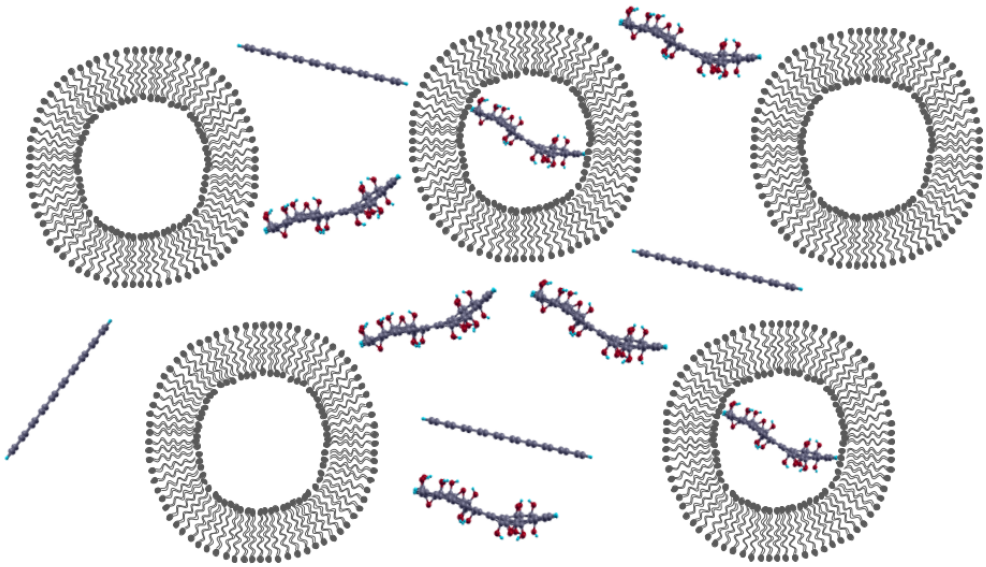

Phospholipids interaction with graphene and graphene oxide

At the interface of quantum calculations and practical experiment

Master's thesis in Biotechnology

VICTOR LANAI

Department of Biology and Biological Engineering
CHALMERS UNIVERSITY OF TECHNOLOGY
Gothenburg, Sweden, 2023

Master's thesis 2023

Phospholipids interaction with graphene and graphene oxide

At the interface of quantum calculations and practical experiment

VICTOR LANAI

Department of Biology and Biological Engineering
Division of Systems and Synthetic Biology
CHALMERS UNIVERSITY OF TECHNOLOGY
Gothenburg, Sweden, 2023

Phospholipids interaction with graphene and graphene oxide
At the interface of quantum calculations and practical experiment

VICTOR LANAI

Supervisor
Shadi Rahimi
Department of Biology and Biological Engineering
Chalmers University of Technology

Examiner
Professor Ivan Mijakovic
Department of Biology and Biological Engineering
Chalmers University of Technology

Master's Thesis 2022 (BBTX60)
Chalmers University of Technology
Department of Biology and Biological Engineering
Division of Systems and Synthetic Biology
SE-412 96, Gothenburg, Sweden
+46 (0)31-772 10 00
www.chalmers.se

Cover:

Typeset in LaTeX
Figures created using XCrysDen

Gothenburg, Sweden, 2023

Phospholipids interaction with graphene and graphene oxide
At the interface of quantum calculations and practical experiment
VICTOR LANAI
Department of Biology and Biological Engineering
Chalmers University of Technology

Abstract

It has been shown that vertically grown graphene flakes are effective in killing bacteria, whilst keeping mammalian cells intact. It was also reported that the graphene oxide sheet can attach to certain drugs and thereby can be used as a therapeutic drug carrier for cancer treatment. However, there is lack of knowledge on the mechanism of interaction between different kinds of cells and graphene-based materials. Therefore, a deeper investigation into the interaction between graphene and the plasma membrane of different types of cells was undertaken. The cell membrane consists of two key components, phospholipids and proteins. Various types of phospholipids exist, and the different types are present in various organisms. Since the constituent of phospholipids seems to differ between bacteria, mammalian normal and cancerous cells, we choose phospholipids as the main target for this thesis. Six phospholipids were studied together with graphene and its derivative, graphene oxide. This thesis is divided into two parts, theoretical and practical parts. In the theoretical part, density functional theory (DFT) is utilized to enhance the understanding at a quantum level. Phospholipids are simulated as isolated single molecules, in pairs and together with graphene and graphene oxide. The theoretical calculations show that the most abundant phospholipids in mammalian cells have stronger bonding to each other, compared to bacterial phospholipids. Further, when the graphene/ graphene oxide sheet is approaching the phospholipid pairs, the bacterial pair exhibits less repulsive interactions, thereby a more stable system with the sheets was found. In the practical part, phospholipids were assembled into liposomes, mimicking a cell membrane and treated with fluorescein functionalized graphene oxide. With fluorescent microscope, we assessed the internalization of graphene oxide by liposomes. Furthermore, differential scanning calorimetry revealed that the constituent of phospholipids affects liposomes heat capacity, which is in line with the theoretical calculations. There would be some other interactions between the cells and approaching material, but we present phospholipids as the key player in this study

Keywords: Phospholipids, graphene, graphene oxide, fluorescein, internalization, heat capacity, density functional theory

Acknowledgements

This has been an amazing experience and I'm very grateful for the opportunity to do this project. This thesis was a collaboration between the departments of Microtechnology and Nanoscience (MC2), and Biology and Biological Engineering at Chalmers University of Technology. I would like to thank Shadi Rahimi, Ivan Mijakovic and Elsebeth Schröder for all your enthusiasm for this project and all valuable support during these months. I greatly appreciate your interest and suggestions for molecules to target. Also, your fantastic guidance through your separate fields opened my eyes for the world of quantum biology and made me appreciate how theoretical- and practical work compliment each other.

I am really looking forward to continuing these collaborations, and believe that together, we push the boundaries.

Victor Lanai
Gothenburg, Sweden, January 2023

Contents

Acronyms

Below is the list of acronyms that have been used throughout this thesis listed in alphabetical order:

a.u	Atomic units
C	Carbon
CL	Cardiolipin
DFT	Density functional theory
G	Graphene
GO	Graphene oxide
H	Hydrogen
HK	Hohenberg-Kohn
KS	Kohn-Sham
N	Nitrogen
O	Oxygen
OH	Hydroxide
P	Phosphorous
PC	Phosphatidylcholine
PG	Phosphatidylglycerol
SCF	Self-consistence field
SE	Schrödinger equation
SM	Sphingomyelin
vdW	Van-der-Waal

Conversions

Ry	13.6056980659 eV
eV	1.60218×10^{-19} J
mol	$6.02214076 \times 10^{23}$ units

Elements

Below is a description of the representative colour of each atom that have been used in figures throughout this thesis:

●	Hydrogen
●	Carbon
●	Oxygen
●	Nitrogen
●	Phosphorous

1
Introduction

It has been showed that vertically grown graphene flakes are effective in killing bacteria, whilst keeping mammalian (eukaryotic) cells intact [1]. It was also reported that graphene oxide sheets can attach to certain drugs and thereby be utilized as a therapeutic drug carrier for cancer treatment. However, there is lack of knowledge on the mechanism of interaction between different kinds of cells and graphene-based materials. One obstacle regards the microscopic size and complexity of cells, and a major challenge is to identify and analyze these interactions in real time. Therefore, we choose to focus our study at one part of the cell, the membrane.

A common feature that all cells share is that they are separated and protected from the outer environment (extracellular space) by a membrane, also known as the plasma membrane, that plays an essential role in diverse cellular functions, including communication and structural rigidity. A major constituent of this plasma membrane is the lipid bilayer. The key component of the lipid bilayer is phospholipids, which represents the most extensive and structurally significant in the lipid bilayer composition, fig.1.1. Alteration in the chemical structure of phospholipid gives rise to a variety of membrane structures, each exhibiting different physicochemical properties [2], and high levels of cellular diversity. Hence, in this thesis, we dive into the constituent of plasma membranes of different cells, and limit our study to the interaction of phospholipids with graphene and graphene oxide. Phospholipids from the outer leaflet of bacteria, mammalian and cancer cells are analysed. The purpose is to investigate if different constituent in the head-group of phospholipids are affecting the interactions with graphene and graphene oxide. We choose to divide this thesis into two parts, theoretical and practical. In the theoretical part, density functional theory (DFT) is utilized to study the interaction of phospholipids with graphene and graphene oxide at a quantum level. In the practical part, phospholipids were assembled into liposomes, mimicking a cell membrane and treated with fluorescein functionalized graphene oxide.

Today, biomolecular simulations are getting recognized as a potential tool in the field of synthetic biology. Computer simulations could help unravel some unknown phenomenons, including the interaction of phospholipids with graphene-based material [3]. However, some of these simulations are still considered as juvenile, and need to be validated by experimental work [4]. Therefore, we chose to combine computational calculations with practical experiment. For the theoretical part, the depth of quantum chemistry is implemented where the electron density of elements are considered as the outcome. Phospholipids are simulated as isolated molecules and in pairs, in combinations relevant for the membranes. Interaction with graphene and graphene oxide into the membrane is also considered. Calculations show that phospholipids from the mammalian cells have stronger bonding to each other, compared to bacterial phospholipids. Further, when the graphene and graphene oxide sheets are approaching the phospholipid pairs, the bacterial pairs exhibit less repulsive interactions, thereby more stable systems with the sheets were found. In the practical part, graphene oxide is functionalized with fluorescein. Liposomes are synthesized from phospholipids, in combinations similar to the theoretical part, followed by treatment with fluorescein functionalized graphene oxide. With fluorescent microscope, we identified internalization of graphene oxide by liposomes. Further, differential scanning calorimetry was performed for the liposomes. This revealed that the constituent of phospholipids affects liposomes heat capacity, which strengthen the interactive pattern seen in the theoretical calculations.

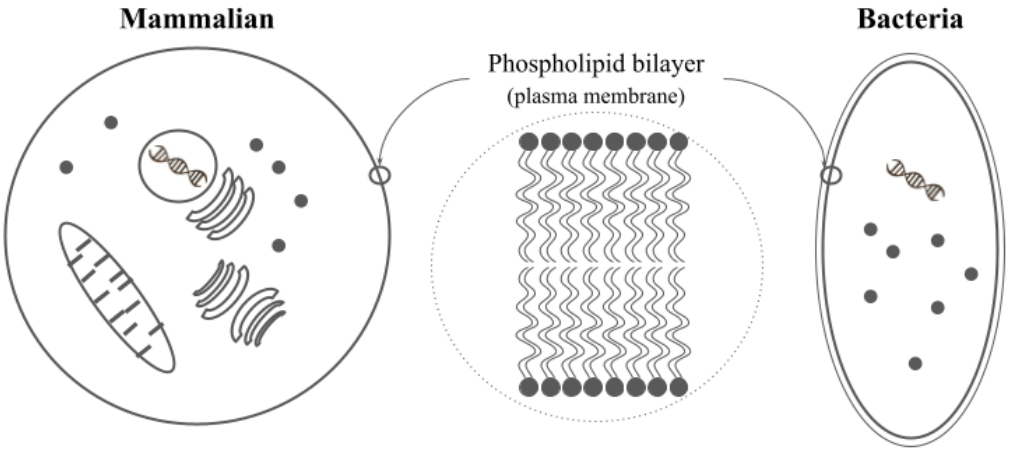

Figure 1.1: Phospholipid bilayer structure in plasma membrane of cells

1.1 Graphene and graphene oxide

Graphene is a 2D layer of single carbon (C) atoms arranged in a honeycomb lattice. It was first isolated in 2004 [5], and has since then attracted much of attention due to its wide range of potential applications. Many sectors are suggested to take advantage of graphene, with the health sector as one potential candidate [6]. In graphene, one C atom is bound to three neighbouring atoms via strong covalent bonds. The remaining electron occupying the orbital perpendicular to the graphene plane creates a free-moving electron, which accounts for the electronic properties. This free-moving electron together with the honeycomb structure is one of the main reasons to the excellent properties of graphene and the promising use in a range of applications [7]. The field of biomedical have exploited graphene and its derivative graphene oxide as a potential candidate, especially in treatment of bacterial induced infection and cancer therapeutics [8]. Regard the bactericidal effect, the orientation of the graphene, and whether its freely suspended or fixed to a surface seems to be a key parameter. It has been shown that vertically grown graphene spikes, coated on top of a surface is bactericidal while being harmless to mammalian cells [1]. However, obstacles remains before it can be fully utilized in the biomedical industry. The biocompatible properties have been debated, mostly related to the hydrophobicity of graphene. This hinders the biocompatibility and utilization of graphene as a drug carrier. But, functionalization of graphene with hydrophilic molecules could enhance the biocompatible properties of graphene. Also, oxidation of graphene is highly useful, generating its derivative, graphene oxide (GO). GO features enhanced hydrophilicity and could therefore be another alternative to increase its water dispersibility [9]. Therefore, both graphene and GO were studied in this thesis. Graphene and GO were incorporated in the theoretical part to calculate its interactions with different phospholipids. For the experimental part, only GO was investigated together with the phospholipids. GO was also functionalized with a fluorescent molecule with the purpose of analyzing its internalization.

1.2 Phospholipid bilayers and liposomes

Lipid membranes are ubiquitous in all cells and are essentially an envelope of phospholipids, embedded with proteins, carbohydrates and cholesterol. All phospholipids are amphiphilic molecules with a hydrophilic ”head” and a hydrophobic ”tail”, fig.1.2. The tail usually consist of two aliphatic chains, derived from fatty acids, where both the length and degree of saturation could differ between different fatty acids. The head comprises of a phosphate group esterified to an organic molecule of varying length and chemical structure [10]. Phospholipids consist of both a water- and a fat loving moiety, which gives them the capacity to self-assemble into phospholipid layers, the heads pointing towards water and the tails attracting each other. Phospholipids can stack into bilayers and aggregate into longer sheets, which forms the majority of plasma membranes [11]. Exposure of the hydrophobic tail to water affects the high free energy, meaning that the phospholipid sheets are closed, giving rise to spherical compartments, called liposomes [12]. Therefore, different concentration of aqueous environment alters the assemble of the supramolecular phase structure, and thus, affects the size and structure of phospholipid bilayers. While all the phospholipids share the common amphiphilic characteristics, they are distinguished by the organic molecule attached to the phosphate group in the head. Also, the length and degree of saturation in the hydrophobic tail could alter, both within the same class of phospholipid but also between different phospholipids. Since the constituent of phospholipids could vary, and particularly between different cell types, it might be a factor to the physical properties and the survival response to graphene ”spikes”.

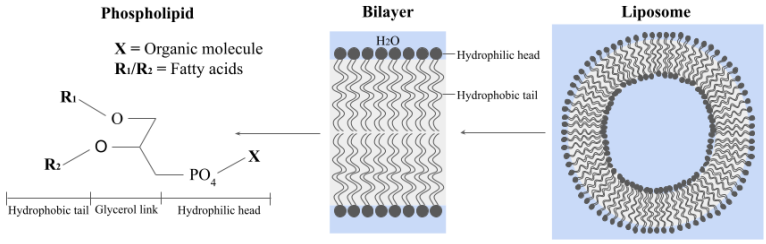

Figure 1.2: Hierarchical structure of liposomes and constituents of phospholipids

In this thesis, two of the most abundant phospholipids in the plasma membrane of bacteria, mammalian and cancer cells where used to mimic and represent the outer leaflet of their plasma membrane. Cardiolipin (CL) and phosphatidylglycerol (PG) represent the bacteria, phosphatidylcholine (PC) and sphingomyelin (SM) represent mammalian, and, phosphatidylethanolamine (PE) and phosphatidylserine (PS) represent cancer cells. The main target of investigation where set to the difference in the constituent of each head group. Thus, the length and saturation of the tail were kept the same in the theoretical part. For the practical part, all phospholipids where obtained as close as possible to mimic the theoretical part, but, some fluctuations in the length and degree of saturation in the tail is inevitable.

1.3 Density functional theory

The computational method in this thesis utilizes the density functional theory (DFT), for which a short overview is given here. DFT is equivalent to the fundamental equation of quantum mechanical systems, the Schrödinger equation (SE)[13][14]. In 1926, Erwin Schrödinger published a series of papers where he postulated "that material points consist of, or are nothing but, wave-systems" and derived this into the mathematical equation

$$\hat{H}\Psi = i\hbar\frac{\delta}{\delta t}\Psi \tag{1.1}$$

which is also called the time-dependent SE [15]. A simplified form for time invariant potentials, is the time-independent, non-relativistic SE

$$\hat{H}\Psi = E\Psi \tag{1.2}$$

where $\hat{H}$ is the Hamilton operator for the system and Ψ is the wave function to a set of eigenstates of the Hamiltonian with the associated eigenvalue E. With variational methods, the solution for the lowest eigenvalue of a stationary state can in principle be found, hence the ground state. Schrödinger set by these expressions the foundation for the future theory of quantum mechanical systems. Both the time-dependent and the time-independent SE are what many scientist in the quantum field have been trying to solve over the years, but exact solutions are not possible for more than a few particles. Therefore, many approaches to these equations have been evolved and one of these is the DFT, which is exact as the time-independent SE, but to solve it for practical purposes, approximations are used. This thesis will not dive into the derivation from the publish of Erwin Schrödinger to the development of the DFT. But, for those who are interested, an historical pathway from SE to DFT is described in Appendix I.

38 years after the publish of SE, Pierre Hohenberg and Walter Kohn published their two Hohenberg-Kohn (HK) theorems [16], and one year later, Walter Kohn and Lu Jeu Sham expanded these theorems into the Kohn-Sham (KS) theorem [17]. These theorems were the birth of DFT and Walter Kohn was awarded the Nobel Prize in chemistry 1998 for his contributions to computational chemistry [18].

The SE contains contributions from all interactive particles within a system, and for a single-particle system, such as the hydrogen atoms, it can easily be solved exactly. But, for a many-body system where multiple particles are interacting, the SE becomes more complicated which makes exact analytical calculations impossible. The major break-through of DFT was the perception of that the ground state of SE is a unique functional of the electron density $n(\vec{r})$.

$$n(\vec{r}) = 2\sum_i \psi_i^*(\vec{r})\psi_i(\vec{r}) \tag{1.3}$$

This lead to the beauty of the KS equation, a one-particle SE for all systems

$$\left[-\frac{\hbar^2}{2m}\nabla^2 + V_{KS}(\vec{r})\right]\psi_i(\vec{r}) = \epsilon_i\psi_i(\vec{r}) \tag{1.4}$$

With $V_{KS}(\vec{r})$ as the KS potential. To solve the KS equation it is necessary to know the single-electron wave function to get the electron density. But to find the single-electron wave function (eq.1.3) the KS equation needs to be solved. To break this circle, Kohn and Sham took advantages of the so called self-consistent field, and the problem was treated by an iterative method. This is done by first defining a trial electron density $n(\vec{r})_{trial}$ and use this to solve the KS equations, which will yield the single-electron wave functions $\phi_i(\vec{r})$. Then, the electron density is calculated from the single-electron wave functions and compared with the initial $n(\vec{r})_{trial}$. If these densities are converging, the ground-state of the system is found. If not, the $n(\vec{r})_{trial}$ must be updated. How this update looks and how to define $n(\vec{r})_{trial}$ together with explanation that tells how accurate the calculations need to be for the densities to converge, is set by different settings in the script that will run the program. This iterative method has also been developed through some years, and today, movement of ions is also allowed, resulting in so-called relaxed state calculations. In this project, both self-consistent field- and relaxed state calculations were performed (fig.1.3). For self-consistent field, the "old" version is applied, and only change of the electronic density takes place, while relaxed state calculations allow movement of the ions as well. Therefore, both the accuracy and computational time for self-consistent field calculations are reduced, compared to relaxed state calculations.

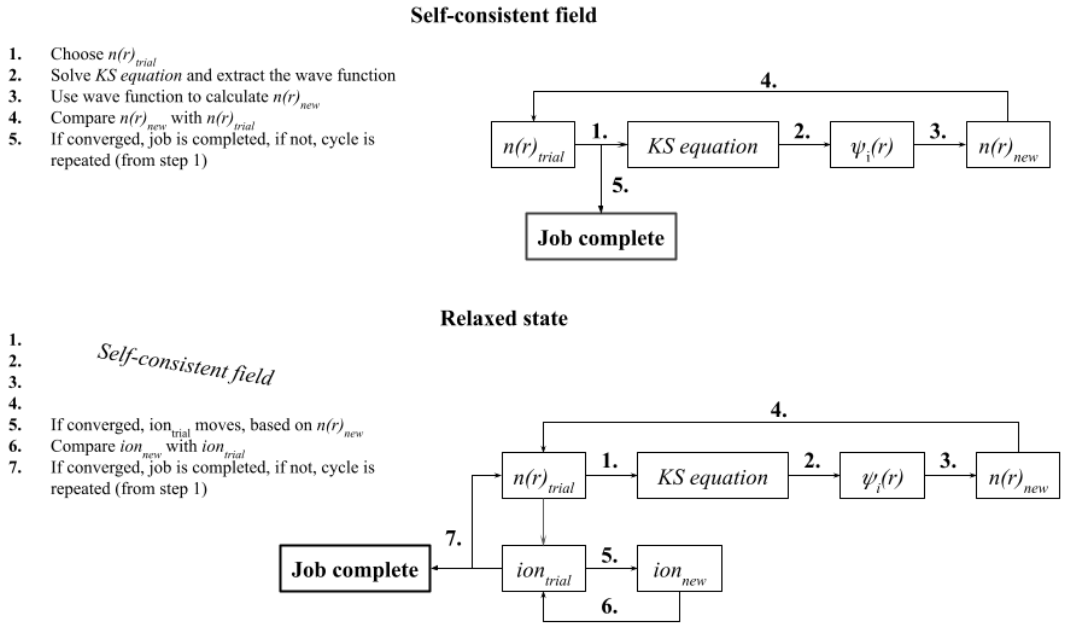

Figure 1.3: Schematic view of the steps in self-consistent field- and relaxed state calculations

2

Theoretical part

This chapter is dedicated to the theoretical part. The first section present the computational methodology, followed by the results. All sections follow the work-flow carried out in this thesis.

2.1 Method and materials

Calculations were carried out by Quantum ESPRESSO, an open source computer code implementation of DFT, plane waves and pseudopotentials [19][20][21][22]. The pseudopotantials (PP) for each atomic specie were picked from the GBRV packages and all the PPs were in unified PP format with the stored potentials as ultrasoft PP and the functional type as PBE [23]. The vdW-DF-cx [24][25][26][27] was used as the input functional for the exchange-correlation which overrides the values from the PP files. Their recommended cutoff kinetic energies for the wavefunctions and charge density where used with values of 40 respectively 200 Ry. All calculations were performed to the relaxed state, except for the system with double phospholipids and graphene/graphene oxide layers, which was set to perform self-consistence field (SCF) calculations. For the k-points, a 2-2-1 Monkhorst-Pack grid was used [28]. All calculations were set to $n_a \times 10^{-7} a.u$ for the electronic selfconsistency threshold, and for the relaxed state calculations, the convergence thresholds for the total energy and forces were set to $n_a \times 10^{-6} a.u$ (n_a = number of atoms).

The constituent and structure for each molecule were collected from the PubChem website [29]. The molecular structures were obtained in 2D and converted to 3D by relaxation. All calculations were carried out with periodically repeated unit cells. To isolate each system from interacting neighbours, a free Bravais-lattice with rectangular base (x,y) and orthogonal height (z) was used, so that all vectors intersected at 90°. The parameters for the unit cells were tailored to fit each system and the concerning molecules. The orthorhombic system is therefore considered and the length of each side will be referred as (x, y, z) Å in the description.

The bonding between molecules was calculated by the formula

$$E_{bond} = E_{tot} - \sum_{i}^{N} E_i \tag{2.1}$$

with E_{tot} as the total energy for the whole system and E_i as the energy from the isolated molecules. The units for the energy in the output-file where given in Rydberg (Ry). The obtained value for $E_{bonding}$ where converged to electron volt (eV) and kilojoule per mol (kJ/mol).

The open source code XCrySDen was used for visualization of the molecular structures. The software shows isosurfaces and contours of the atoms which can be interactively manipulated through rotation, colours, atomic radii and thickness of bonds [30].

2.1.1 Graphene and graphene oxide

The precise chemical structure of GO has been debated over the years and there is still no unambiguous model existing. This could be due to the lack of suitable analytical techniques for characterization, but also the fluctuation between different samples. The edges for the non-periodic sides for both graphene (G) and GO were structured as a zigzag pattern with H atoms bonding to the edges [31]. The prediction of the distribution of functional groups on the GO layers was influenced by Anton Lerf and Jacek Klinowski, who published a model that has become the most well known today [32]. The constituents of the GO layer were obtained from the graphene supermarket [33]. The composition was specified to 79 weight% C and 20 weight% O. According to the Lerf-Klinowski model, most of the oxygen atoms are attached as epoxy-(-O-) and alcohol groups (-OH) [34]. It was therefore assumed that the rest (1 weight%) belonged to H atoms. The distribution of weight% was

transferred into number of atoms/carbon. This was done by the following steps:

The Molar mass of each atom is

$$M_H = 1.008 \text{ g/mol}, \quad M_C = 12.011 \text{ g/mol}, \quad M_O = 15.999 \text{ g/mol} \tag{2.2}$$

and the equation for weight% can be written as

$$\frac{12.011 n_C}{m_T} = 0.79, \quad \frac{15.999 n_O}{m_T} = 0.20, \quad \frac{1.008 n_H}{m_T} = 0.01 \tag{2.3}$$

With n_i as the number of mols, M_i as the molar mass and m_T as the total mass. The formulas of Eq.2.3 were rearranged and the distribution of number of atoms were given as

$$\frac{n_O}{n_C} = 0.19, \quad \frac{n_H}{n_C} = 0.15 \tag{2.4}$$

The cell sizes for both flakes were set to (30.00, 8.00, 14.76) Å

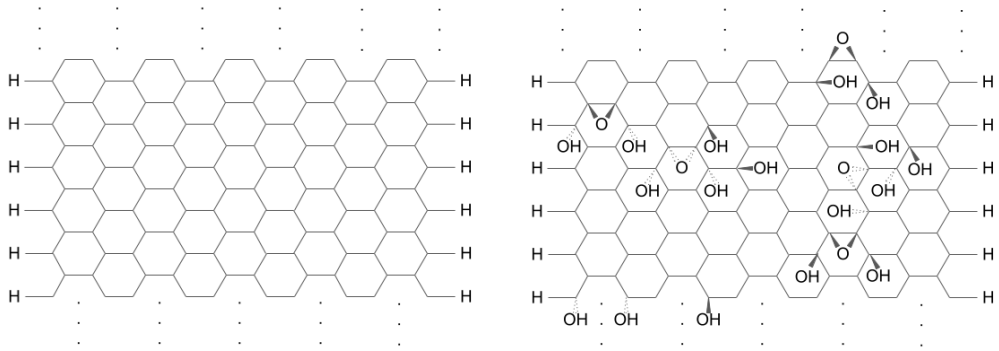

(a) G (b) GO

Figure 2.1: The initial 2D structures of the calculated flakes. The atom distribution from (a) G, and (b) GO, where dots at the top and bottom represents the periodicity

2.1.2 Phospholipids

A small library of six isolated phospholipids was created, fig.2.2. They were hand-picked by their abundance in each organism. Phosphatidylglycerol (PG) and cardiolipin (CL) are two major constituents in bacteria membranes [35]. The outer leaflet of human membranes have high levels of phosphatidylcholine (PC) and sphingomyelin (SM) [36][37] while the concentration of phosphatidylethanolamine (PE) and phosphatidylserine (PS) are higher in outer leaflet of cancer cells [38].

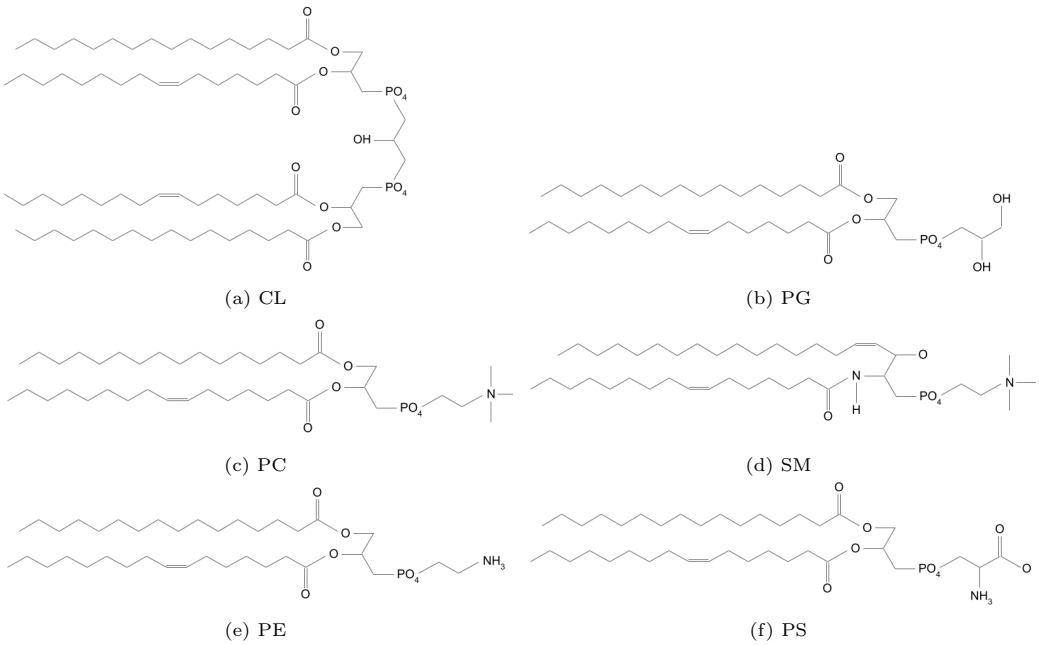

(a) CL (b) PG

(c) PC (d) SM

(e) PE (f) PS

Figure 2.2: 2D structures of each phospholipid which was computed in this thesis

Calculations started by simulations of the ”heads” from each phospholipid together with two carbons of each acyl chain (the ”tail”). When the optimal state of each head-group was reached, the rest of the tails were introduced. Each phospholipid were simulated with one saturated (16:0) and one unsaturated (18:1) lipid in the tail. The initial 2D The cell parameters were set to (40.00, 20.00 , 15.00) Å for isolated PC, PE, PG, PS, SM and (40.00, 40.00, 15.00) Å for CL.

The single phospholipids were simulated together with a second phospholipid from the same organism, for analysis of the interactive energy between different phospholipids. In plasma membranes, multiple phospholipids interact in a parallel manner, but the exact positions (rotations) between phospholipids is not defined. Therefore, we assume parallel stacking in the horizontal direction (from the tail to head), and all rotations of the horizontal axis of each phospholipid is allowed. In this project, the initial positions of the paired phospholipids, CL/CL, CL/PG, PC/PC, PC/SM, PE/PE, PE/PS, PG/PG, PS/PS and SM/SM, were obtained by introducing one single phospholipids into another single phospholipid. We define two terms of stacking, the z- and y-stacking. For both systems of stacking, one of the phospholipids was moved 10.00 Å in y- and z- direction respectively. The cell parameters were set to (40.00, 25.00, 15.00) Å for the y-stacking and (40.00, 25.00, 25.00) Å for the z-stacking.

2.1.3 Incorporation of graphene and graphene oxide to the phospholipid systems

Analysis of the interaction between the phospholipid pairs to the G/GO flakes were also calculated. These simulations were performed with SCF calculations via a number of steps. First, calculations of approaching G/GO flakes to the head groups of the phospholipid pairs were performed. The y-stacking systems with cis tails were representing the each phospholipid pairs. The zero distance of the G/GO layers in the x-direction, was set so that the lowest x-value in the G/GO layers were perpendicular to the highest x-value of the phospholipid pair. In y-direction, the initial position were set as the average y-value of the phospholipid pairs, so that the flake were set as close as possible to ”the gap” of interactive heads. Eight steps were calculated, from 7 Å down to 0 Å in the x-direction. The cell parameters were tailored for each system, so that the no interaction took place between repeated cells.

2.1.4 Constrains

Important highlights are the complexity of cells and the computational effort. One fundamental limitation of DFT is the association between number of atoms and time for calculation. Another challenge is an accurate description of the environment. Therefore, certain boundaries have been set in this project. All calculations have been performed at 0 K. The systems have also been set to perform relaxed- or self consistent field (SCF) calculations. Calculations for the relaxed state allow movements of both electrons and ions, until the optimal structure is found. SCF calculations keep the ions fixed, and only movement of electrons is allowed, which leads to less accurate outcome but a decrease in computational time. Therefore, to reach some results within a reasonable time frame, relaxation were performed to describe isolated system, id est, pairwise phospholipids and isolated G/GO layers. SCF calculations were performed with the purpose to analyze the isolated systems together, id est, interactions between phospholipid pairs and a G/GO layer.

2.2 Results and discussion

This section presents results from the SCF- and relaxed state calculations, and the sections follow the work-flow of the project. First, the relaxed state of each phospholipid in a single isolated form is illustrated. These single isolated phospholipids were used as the initial molecular structures for simulation of the phospholipid pairs to relaxation, and results from these calculations are presented in the following section. The last section includes results from G/GO interactions with the paired phospholipids, which were all performed with SCF calculations.

2.3 Single Phospholipids

This section presents the outcome from the relaxed state calculations of each single phospholipid. Fig.2.3 illustrates the isolated phospholipids that were used as the initial molecular structure for the system of phospholipid pairs.

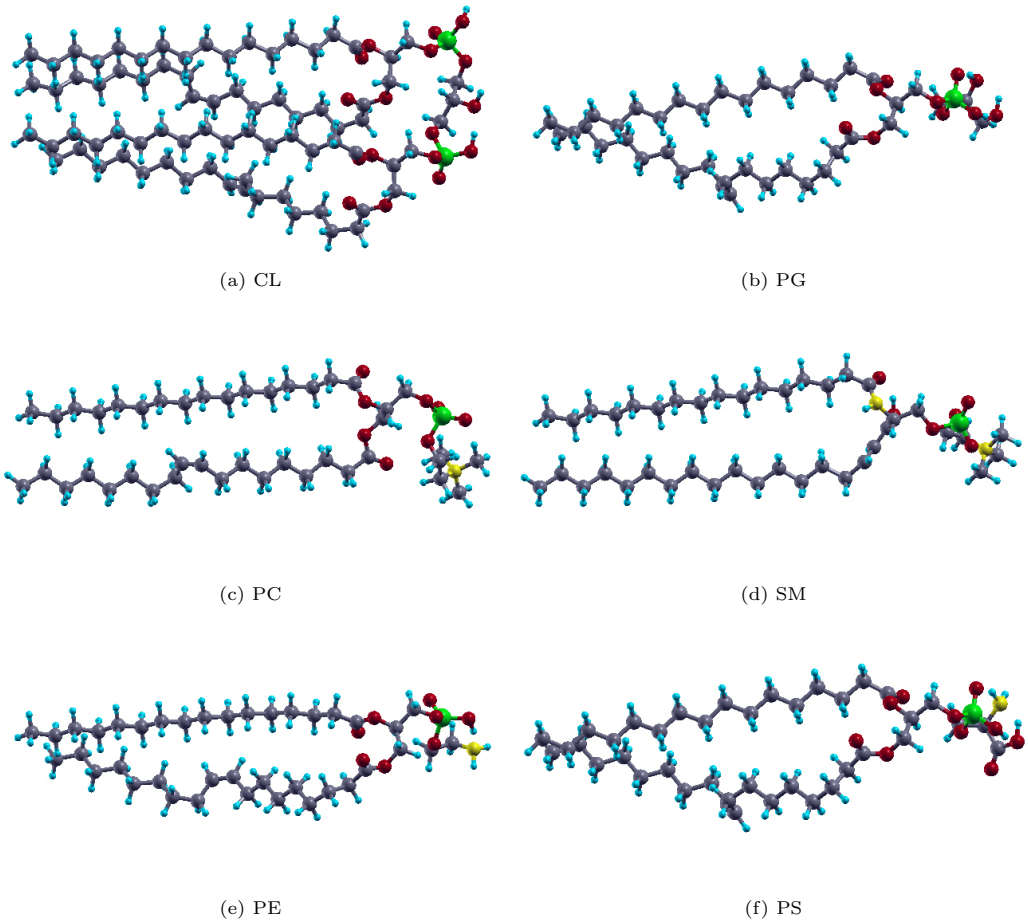

(a) CL (b) PG

(c) PC (d) SM

(e) PE (f) PS

Figure 2.3: Visualization of the optimal structure of each phospholipid

2.4 Phospholipid pairs

The single phospholipids were put together into systems of pairs, and further relaxed, fig.2.4. PC/PC, PC/SM and SM/SM were simulated as the mammalian plasma membrane, and PG/PG, CL/CL and CL/PG were created as the bacterial membrane, while PE/PE, PE/PS and PS/PS represented the cancer cell membrane. Stacking of the bacterial pair seems to be straighter with a larger gap between them, while the mammalian pairs stacks closer to each other with tilting head-groups. For the PC/SM and PE/PE pairs, an overlap in the hydrocarbon tails also takes place, which could allow for a denser stacking.

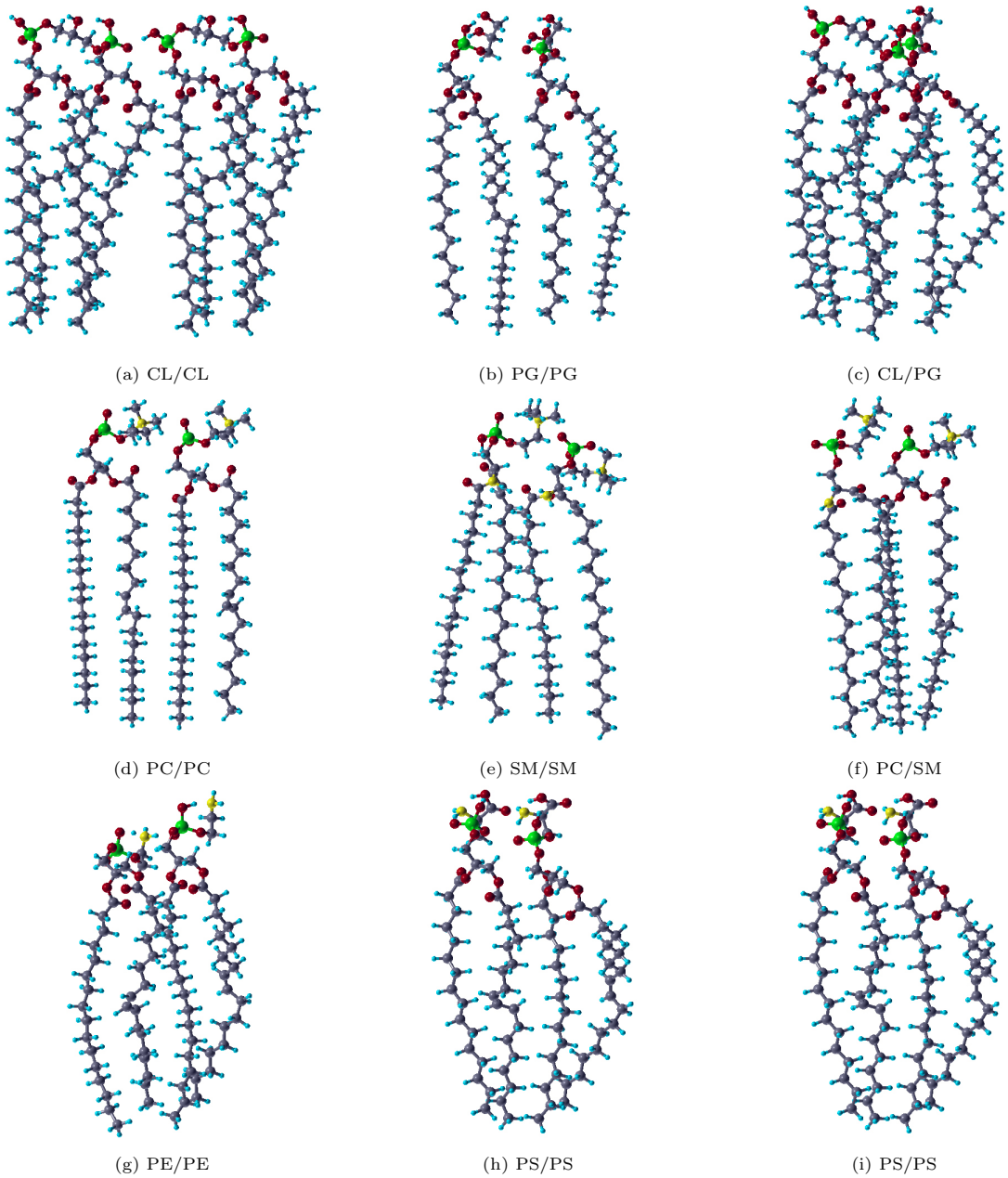

(a) CL/CL (b) PG/PG (c) CL/PG

(d) PC/PC (e) SM/SM (f) PC/SM

(g) PE/PE (h) PS/PS (i) PS/PS

Figure 2.4: Visualization of paired phospholipids

Table.2.1 shows the obtained energies between the interacting phospholipids. Energies between phospholipids of mammalian cells are more negative than for bacterial phospholipids. Presence of sphingomyelin seems to lower the energy, with SM/SM as the strongest interaction in the mammalian pairs. For all systems, the environ plug-in cause a decrease in energy, which could be explained by the hydrophilic and hydrophobic properties, where presence of water pushes the hydrophobic tails closer to each other, which allow for more and stronger interactions.

Table 2.1: Interaction energy between paired phospholipids in vacuum and environ.

Organism	Phospholipid pair	Stacking direction	Energy in vacuum [kJ/mol]	Energy in environ [kJ/mol]
Bacteria	CL/CL	y stacking	-101	-236
	CL/CL	z stacking	-188	-273
	PG/PG	y stacking	-52	-111
	PG/PG	z stacking	-157	-236
	CL/PG	y stacking	-113	-185
	CL/PG	z stacking	-140	-238
Mammalian	PC/PC	y stacking	-120	-135
	PC/PC	z stacking	-186	-258
	SM/SM	y stacking	-203	-248
	SM/SM	z stacking	-231	-263
	PC/SM	y stacking	-165	-207
	PC/SM	z stacking	-188	-245
Cancer	PE/PE	y stacking	-141	-194
	PE/PE	z stacking	-151	-219
	PS/PS	y stacking	-107	-170
	PS/PS	z stacking	-165	-239
	PE/PS	y stacking	-102	-178
	PE/PS	z stacking	-194	-216

Fig. 2.5 shows the interactive energies in a scatter plot. First, the cancer pairs are in range with the mammalian, which is expected since the cancer cells are derived from mammalian cells. For the z-stacking pairs with the environ plug-in, the interactive energies becomes more homogeneous between the pairs. An explanation to this could be that z-stacking allows for more interactions between the tails, and thus, the contribution from the heads becomes less significant. For the bacterial systems, CL lowers the interactive energies, which is not very strange, since CL contains almost twice as many atoms in the tail compared to PG, the number of interactions between the phospholipids increases, and thus, the energy decreases.

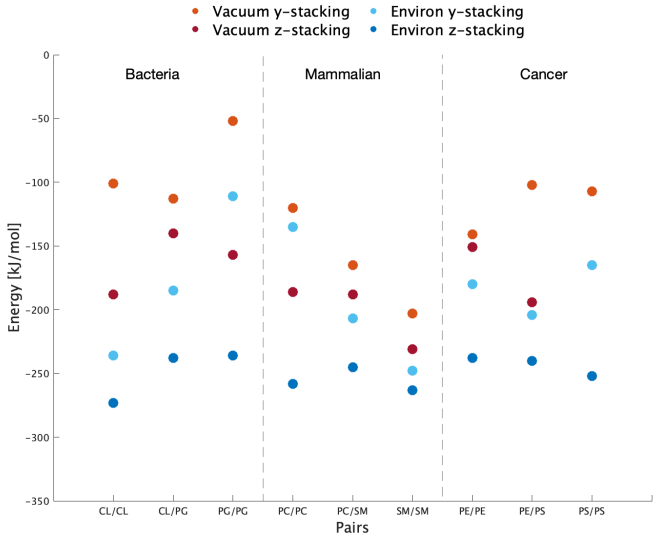

Figure 2.5: Plot of the interactive energy between paired phospholipids. Orange and red represent vacuum, while light- and dark blue shows calculations with the environ plug-in.

2.5 Graphene/graphene oxide interactions with paired phospholipids

Approaching of the G/GO flakes to each phospholipid pair was studied by calculating the interaction energy between G/GO and the phospholipid pair at different distances, as illustrated in fig.2.6.

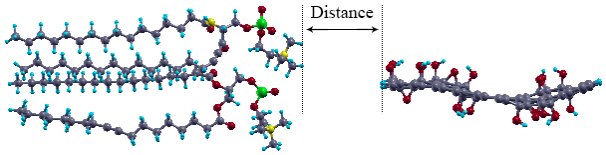

Figure 2.6: Visualization of approached graphene oxide flake to one of the phospholipid pairs

In fig. 2.7, the interaction energies of the phase of G/GO approaching the heads of the phospholipid pairs are plotted. Negative values (y-axis) represent attractive forces between the head of the phospholipids and the G/GO layer. When G/GO approaches the lipid pair, energies are increasing and positive values are found, which indicate repulsive forces. Since these systems are evaluated by SCF calculations, ions cannot move, and thus, the repulsive forces are expected. For the bacterial systems, the most stable (lowest energies) distance is around 1 Å, while the mammalian systems shows high repulsive forces at this distance. The pairs representing cancer, one of the systems are similar to the mammalians, while the other two allow closer approaching of the flakes. The major difference between G and GO is that the repulsive response takes place at a longer distance with GO approaching. GO has functional groups attached to the surface, which might interact with the head of the phospholipids further away, compared to the pure G layer.

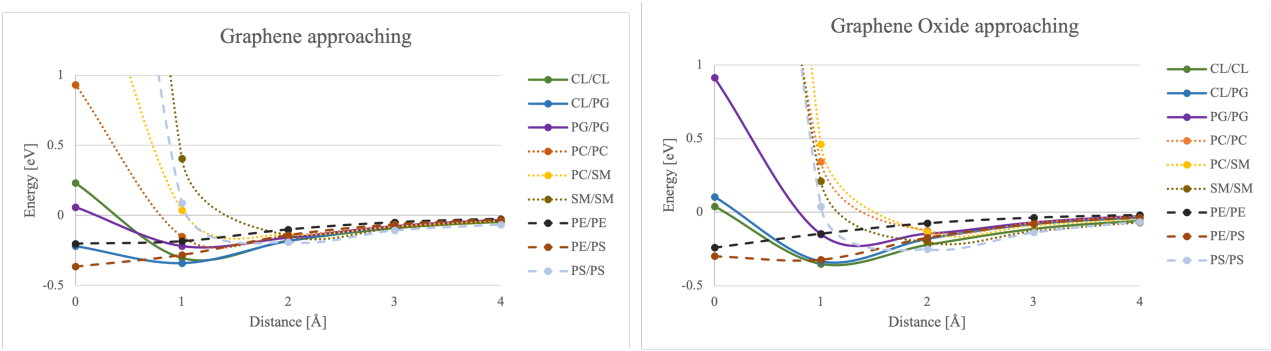

(a) G approaching paired phospholipids

(b) GO approaching paired phospholipids

Figure 2.7: Interaction energy when a) G and b) GO approach paired phospholipids.

3

Practical part

In this chapter, the methodology and outcome from the practical experiments are presented. First, GO sheets were functionalized with fluorescein. Next, phospholipids were assembled into liposomes, followed by treatment with the fluorescein functionalized GO sheets. Analysis was performed to confirm functionalization of GO. The effect of phospholipid concentration on the size of liposomes was analyzed, with the purpose of finding suitable size reflecting the cell membranes. Differential scanning calorimetry was also performed for each liposome, and the calculated heat capacities were fitted into the theoretical calculations.

3.1 Material and methods

3.1.1 Material

The graphene oxide was obtained from the graphene supermarket. Fluorescein, 1,1'-Carbonyldiimidazole (CDI), Poly(ethylene glycol), dimethylsulfoxide (DMSO), 18:0/1 cardiolipin (CL), egg/soy phosphatidylcholine (PC), 16:0-18:1 phosphatidylethanolamine (PE), egg/18:0 phosphatidylglycerol (PG), soy phosphatidylserine (PS), brain sphingomyeline (SM) were obtained from Merck.

3.1.2 Graphene oxide functionalization

Functionalization was done according to previous described method [39]. First, 2.5 mg GO-sheets were diluted in 25 mL of DMSO and then sonicated for 1h. The solution was then reacted with 2.5 mg CDI at 40 °C, for 2h with stirring, and then centrifuged at 10 000 rpm for 30 minutes. The precipitate was collected and resuspended in DMSO, then reprecipitated again by centrifugation. Next, the GO-CDI solution was diluted with 25 mL of DMSO and mixed with 5 mg of PEG 2000 under stirring for 24h at 40°C. The suspension was then centrifuged at 10000 rpm for 30min and the supernatant was removed. The resuspended precipitate was subsequently dialyzed (7000 Da MWCO, SpectrumLabs Spectra/Por Biotech CE membrane) for 5 days to remove excess PEG 2000. Finally, 2.5 mg fluorescein and 2.5 mg CDI were allowed to react in 2.5 mL DMSO under stirring at 40°C for 2h. Next, this CDI-activated fluorescein was mixed with the suspension of PEG-modified GO sheets with stirring for 24h at 40°C. The suspension was dialyzed for a week to remove any fluorescein that was not covalently bound with GO. The final solution was centrifuged at 10 000 rpm for 30 minutes, followed by removing the supernatant. The precipitate was resuspended in deionized water and the functionalized GO (GO-F) concentration was determined to 50 $m g m$L.

3.1.3 Fluorescent properties

SPECTROstar Nano with Costar 96 well plate was used to measure the absorbance spectra. 2.5 mg fluorescein was mixed in 1 mL of deionized water and 1 mL of DMSO respectively. The absorbance was measured for three replicates per samples. Each well contained 200µL of solution. The absorbance spectra was measured between 350-550 nm. The mode was set to kinetic, with 3 numbers of cycles and a cycling time of 50 s.

FLUOStar Omega with Costar 96 well plate was used to measure fluorescent emission. Wavelength from excitation and emission was set to 485 nm and 520 nm respectively with the optic set to top. Mode was set to endpoint and 2 multichromatics were measured with a gain of 500 and 1000. Orbital average was set to 2 with a setting time of 0.5 s. Measurement start time was set to 0 with 17 number of flashes per well. Three replicates were measured per sample. Each well contained 200µL of solution.

3.1.4 Preparation of liposomes

All phospholipids were obtained as powders and suspended in ethanol, yielding stock-solutions of phospholipids with a concentration of 25 and 50 mg/mL. The stock-solutions were stored at minus(-) 20 degrees °C. Liposomes

were prepared by the hand-mixing procedure [40]. In the first step of liposome assembly, the phospholipid stock-solutions were further diluted in ethanol to a concentration of 5 mg/mL and 10 mg/mL. Final, the ethanolic phospholipid solutions were transferred into Milli-Q water, with a 1:1 and 3:1 ratio (H2O:EtOH), and mixed for 30 seconds with pipetting.

3.1.5 Size distribution

Dynamic light scattering (DLS) was performed with a ZETASIZER Nano series from MALVERN Intstruments with DTS0012 disposable cuvettes. 1 mL of sample was analyzed to determine size distribution after synthesis. Refractive index for the liposomes was set to 1.45. 1%EtOHinwater was set as dispersant, with a viscosity of 1.0193 cP and refractive index of 1.330. Temperature was set to 21°C, with an equilibration time of 10 s. Measurement angle was set to default (173°Backscatter). 3 measurements were performed for each sample with 3 numbers of runs and a run duration of 10 s for each measurement. Delay between measurements was set to 0.

3.1.6 Thermogravimetric analysis/Differential scanning calorimetry

A STA 409 PC Luxx from NETZSCH was used for simultaneous thermogravimetric- and differential calorimetric analysis (TGA/DSC). Liposomes synthesized from a phospholipid concentration in ethanol solution of 20 mg/mL, and 1:1 (H2O:EtOH) ratio were used (final concentration of 10 mg/mL). 40 µL from each sample was heated from 25-70 °C with a scan rate of 1 °C /min. The endothermic peaks at 25-38°C were analyzed, and the area under the curve were calculated as the heat capacity. The baseline was set to zero and everything above zero was considered as a part of the endothermic peaks.

3.1.7 Liposome treatment with functionalized fluorescein GO

After the DLS measurement of the liposomal sizes, it was concluded that 10 mg/mL and 1:1 (H2O:EtOH) ratio gave the highest particle sizes. Since the purpose of liposome preparation is to mimic the cell membranes, high particle sizes are aspired. Therefore, liposomes synthesized from a phospholipid concentration in ethanol solution of 10 mg/mL, and 1:1 (H2O:EtOH) ratio were used. Two procedures were performed for liposome treatment with functionalized fluorescein GO. One procedure is to treat all liposomes in single and mixed format similar to the theoretical calculations, while the other procedure is to treat selected bacterial and mammalian liposomes with similar formulation to bacterial and mammalian membranes.

For the first procedure of liposomes treatment, the liposomes were treated with 2 mg/mL of GOF, followed by incubation for 1 h at 37°C. 5 µL of each sample was analyzed with LeicaCTR4000 confocal fluorescent microscope for evaluating GO-F internalization.

For the second procedure of treatment, selected bacterial and mammalian liposomes were assembled and treated with functionalized fluorescein GO. The bacterial liposome contained 20 weight% CL and 80 weight% PG [41], while the mammalian liposome was assembled with 45 weight% PC, 45 weight% and 10 weight% PE [42]. Three samples were synthesized for each type of liposome. The liposomes assembled in a total volume of 300 µL and treated with 5 mg/mL of the functionalized fluorescein GO, followed by incubation for 6 h at 37 °C. After treatment, the liposomes were separated from the liquid solution by solvent-based precipitation [43]. For this, 300 µL EtOH was added to the treated liposomes from previous step and mixed for 10 min, followed by low-speed centrifugation, 4700 g for 10 min. The supernatant was removed, and the precipitates were air-dried for 30 min at room temperature, followed by drying at room temperature in vacuum for 1 h. The dried pellets were resuspended in phosphate buffer saline (pH 7.4) and vortexed for 30 s. Fluorescent emission was measured by FLUOStar Omega with Costar 96 well plate. Wavelength from excitation and emission was set to 485 nm and 520 nm respectively with the optic set to top. Mode was set to endpoint and 2 multichromatics were measured with a gain of 500 and 1000. Orbital average was set to 2 with a setting time of 0.5 s. Measurement start time was set to 0 with 17 number of flashes per well. Three replicates were measured per sample. Each well contained 100 µL of solution.

3.2 Results and discussion

3.2.1 Graphene oxide functionalization

Before removal of the DMSO and resuspention of water took place, the following method did not mention this last step, and thus, the final suspension was first considered in DMSO. However, after the last step of synthesise, no fluorescein was noticed. According to literature, the fluorescent properties of fluorescein is highly pH dependent [44], and thus, the effect from DMSO was analyzed. As the first step, fluorescein powder were diluted in DMSO and H_2O respectively to measure the absorbance. Fig. 3.1 shows a clear shift in absorbance spectra between fluorescein in H_2O and DMSO. The absorbance spectra of fluorescein in H_2O follows literature [45], while absorbance spectra for fluorescein in DMSO is absent.

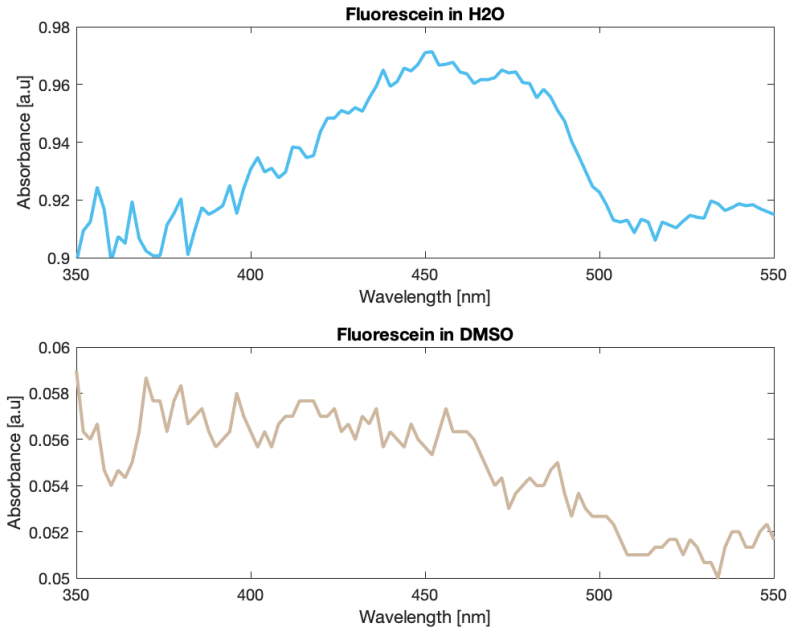

Figure 3.1: The absorbance spectra for fluorescein in water and DMSO.

Next, DMSO was removed from the functionalized fluorescein GO (GO-F) solution and respunded in H_2O. Fluorescent intensities were measured for GO-F in H_2O, GO-F in DMSO and pure GO in H_2O. Fig.3.2 shows that only GO-F in H_2O give fluorescent properties, and thus, the functionalization was probably a success, and that the solvent highly effects the fluorescent properties.

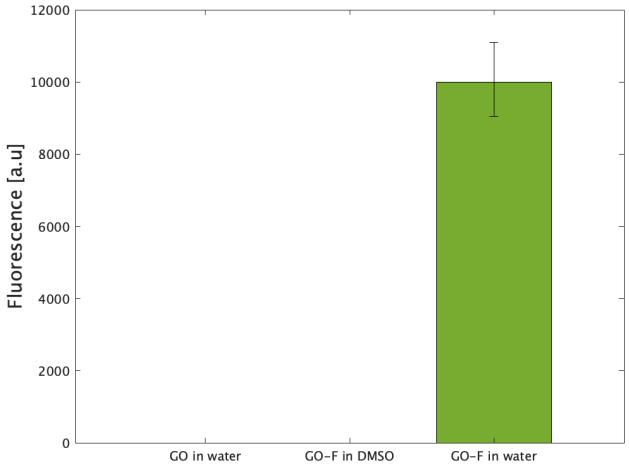

Figure 3.2: Measured fluorescence from the functionalized GO flakes in water and DMSO, together with measurement for pure GO in water.

After that, the size distribution of GO-F was measured. This were also done for the original GO and sonicated GO. Fig.3.3 shows that the original GO possess the largest size, while sonicated flakes display the smallest flakes, which is as expected after sonication. GO-F exhibits larger particle size than the sonicated, which could confirm attachment of molecules and thus, confirm the functionalization.

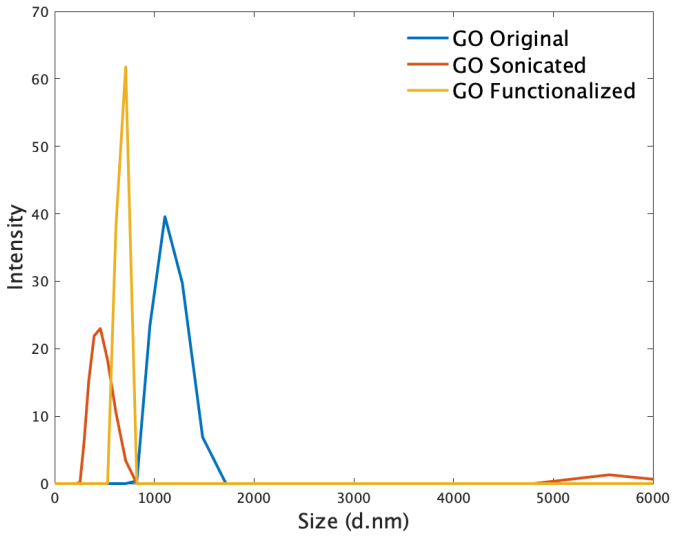

Figure 3.3: Size distribution from dynamic light scattering of functionalized GO, sonicated GO and original GO.

3.2.2 Liposome sizes

As the first step of liposomal synthesise, the effect from phospholipid concentration and H_2O:EtOH ratio were investigated, and their effect on particle size. Two concentrations of phospholipids in ethanol, and two ratios of H_2O:EtOH were analyzed. The assemble of phospholipid mix followed the theoretical calculations, thus, liposomes were synthesized from 100% CL, 50/50% CL/PG, 100% PG, 100% PC, 100% SM 50/50% PC/SM, 100% PE, 100% PS and 50/50% PE/PS. Together with the variables for particle size (concentration and H_2O:EtOH ratio), this yielded in 36 samples. The particle size for all samples were measured, stored at -20°C for 24h and then remeasured. The primary goal was to analyze the size distribution, and the secondary goal was to confirm if storing effects the sizes. Each peak from the DLS measurement was extracted and plotted against phospholipid concentration and H_2O:EtOH ratio, fig. **??**. This shows that both higher initial phospholipid concentration and lower H_2O:EtOH ratio increases the size. After storing the liposome over night at -20°C, they displayed similar size distribution 3.5.

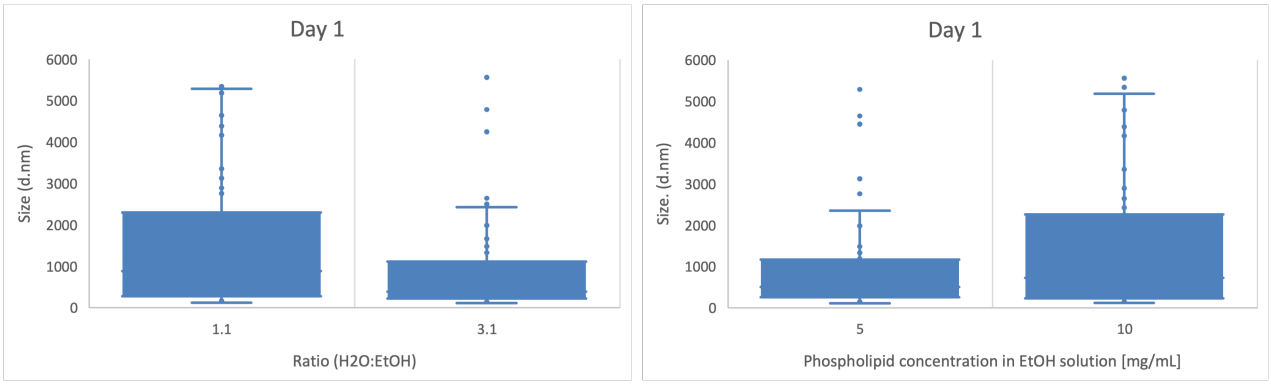

(a) (b)

Figure 3.4: Extracted peaks from the DLS measurements with respect to (a) H_2O:EtOH ratio, and (b) phospholipid concentration in EtOH solution.

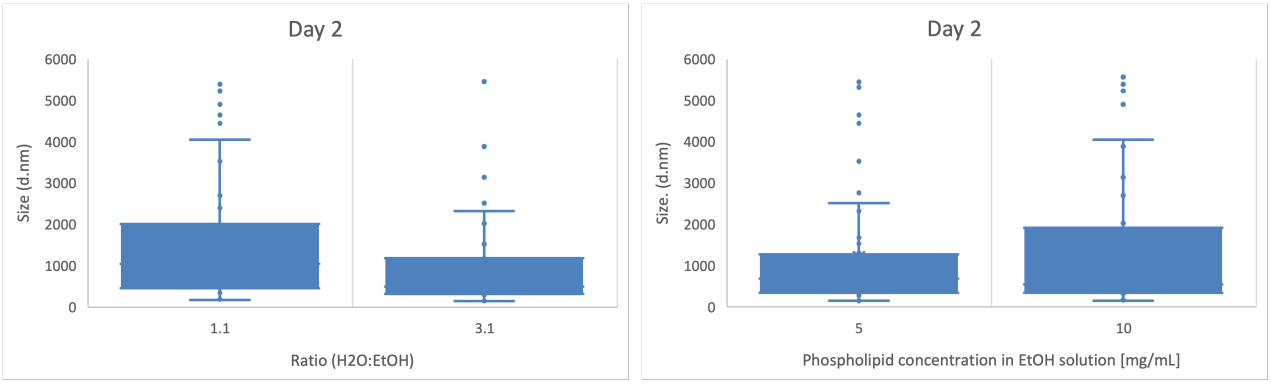

(a) (b)

Figure 3.5: Extracted peaks from the DLS measurement of liposomes after storing at -20 °C for 24h. Boxplot with respect to (a) H_2O:EtOH ratio, and (b) phospholipid concentration in EtOH solution.

In this project, the purpose of liposomes are to mimic the plasma membranes in cells, therefore, larger particles are desired. Thus, we choose an initial phospholipid concentration of 10 mg/mL and 1:1 H_2O:EtOH ratio for the liposomal treatment with GO-F. The size distribution from these conditions are presented in fig.3.6. A first glimpse indicates that the bacterial liposomes forms larger particles, but, from microscopic images it can be viewed as aggregation of smaller particles. The sizes from the mammalian and cancer liposomes are spotted as more alike, while the mammalian liposomes exhibits the most uniform distribution.

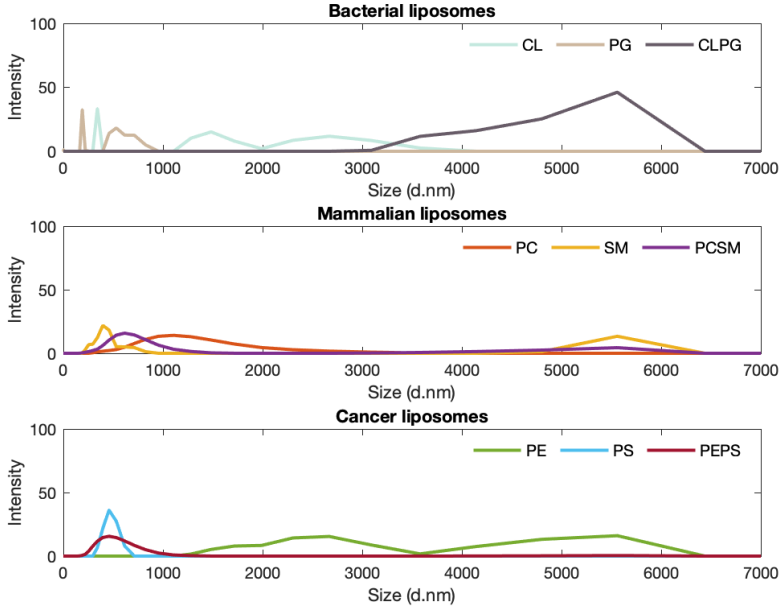

Figure 3.6

3.2.3 Evaluation of liposome treatment with functionalized GO

The main purpose of liposome treatment with functionalized GO were to investigate whether graphene oxide can internalize into the liposomes or not, and if there is any difference between phospholipid composition. Treatment was done under incubation at 37 °C for 1 h, to mimic the optimal conditions for most bacteria and mammalian cells. Fig.3.7a,3.7b and 3.7c shows images from the fluorescent microscope. First, we can confirm the statement above, two of three bacterial liposomes are small with a tendency to aggregate (100% CL and 50/50% CL/PG), fig.3.7a, and, no internalization were visualized for these liposomes. However, some internalization was found for liposomes with 100% PG. For mammalian liposomes, nothing significant took place for the 100% PC and 100% SM, but, in the 50/50% mix, internalization were visualized, fig.3.7b. The liposomes of cancer displayed most internalized GO-F flakes fig.3.7c.

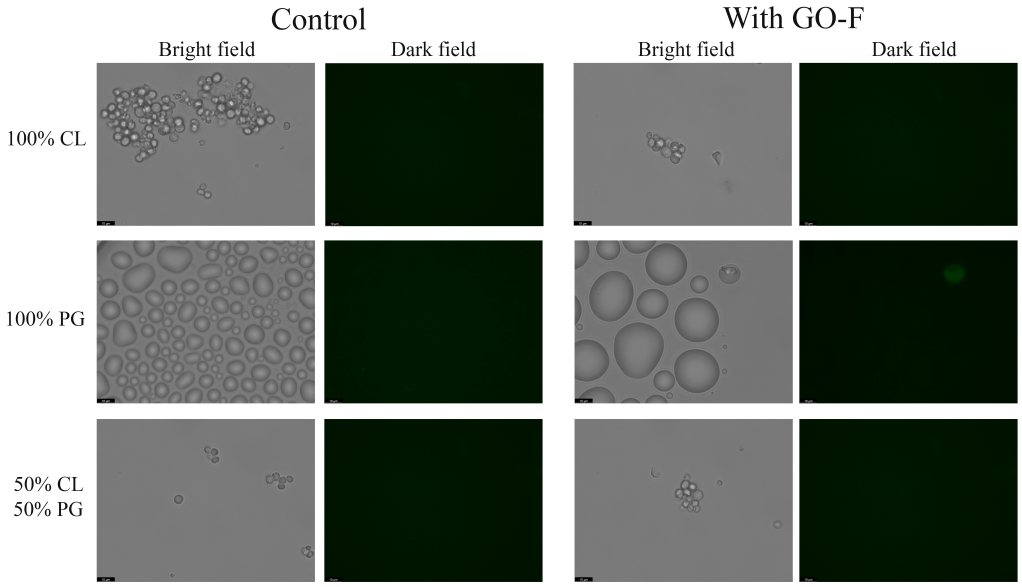

(a) Bacteria liposomes. Images from fluorescent microscopy of liposomes after treatment with GO-F

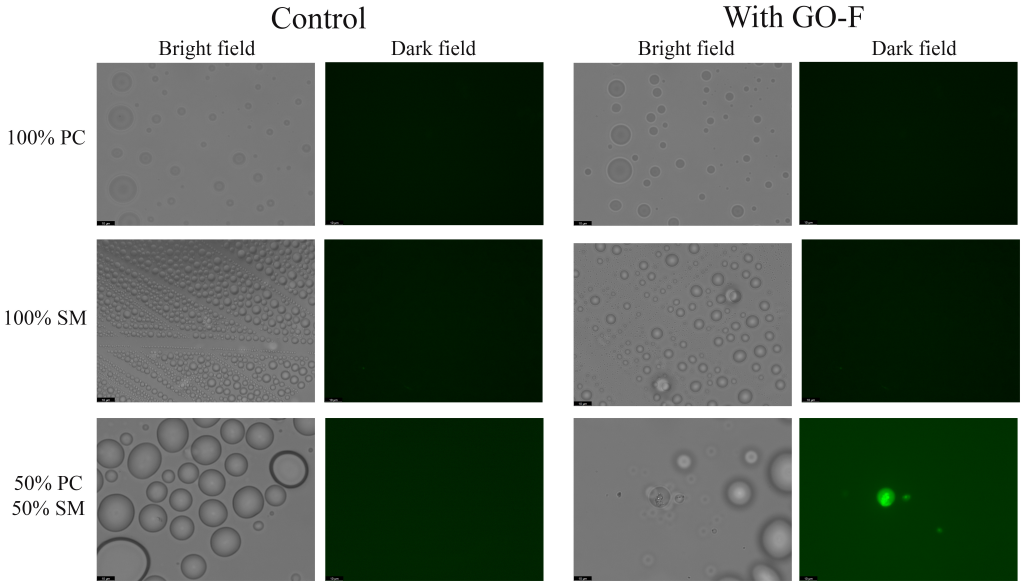

(b) Mammalian liposomes. Images from fluorescent microscopy of liposomes after treatment with GO-F

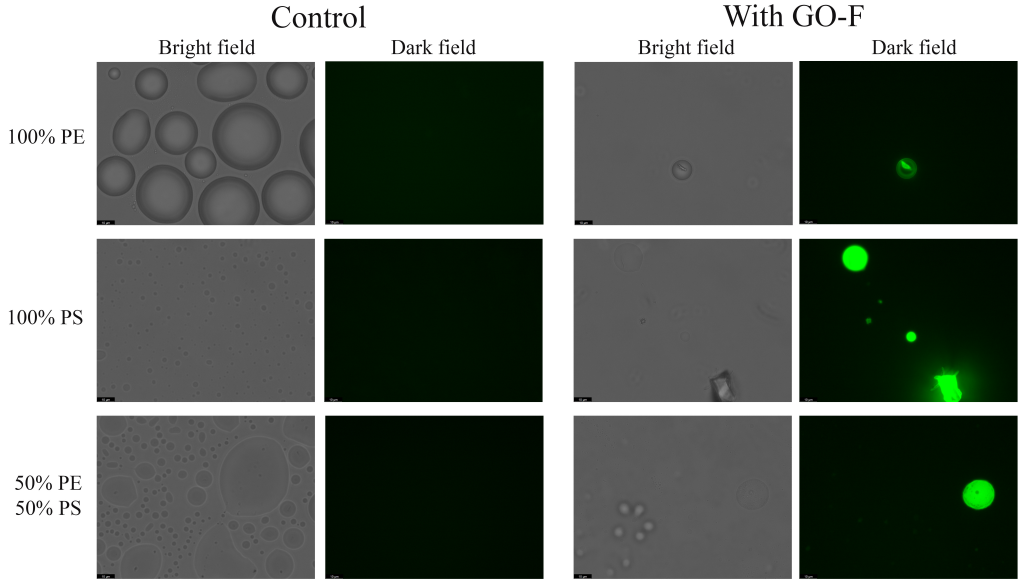

(c) Cancer liposomes. Images from fluorescent microscopy of liposomes after treatment with GO-F

Next, for the quantitative assay, selected bacterial and mammalian liposomes as the representatives of bacterial and mammalian membranes were treated with the GO-F. In fig.3.8 we can see a higher fluorescent signal from the mammalian liposomes, which indicates more internalization of the GO-F. This follows the pattern from the fluorescent microscope, which insinuated more internalization of the GO-F into the mammalian liposomes. If we connect this to the theoretical part, it was shown in the SCF-calculation that approaching GO flakes exhibited less repulsive forces to bacterial phospholipids compared to the mammalian. Less fluorescent signal from the bacterial liposomes can be interpreted that GO-F penetrates and disrupt the bacterial liposomes, while the mammalian liposomes allow less membrane penetration and more internalization when the membrane remains intact.

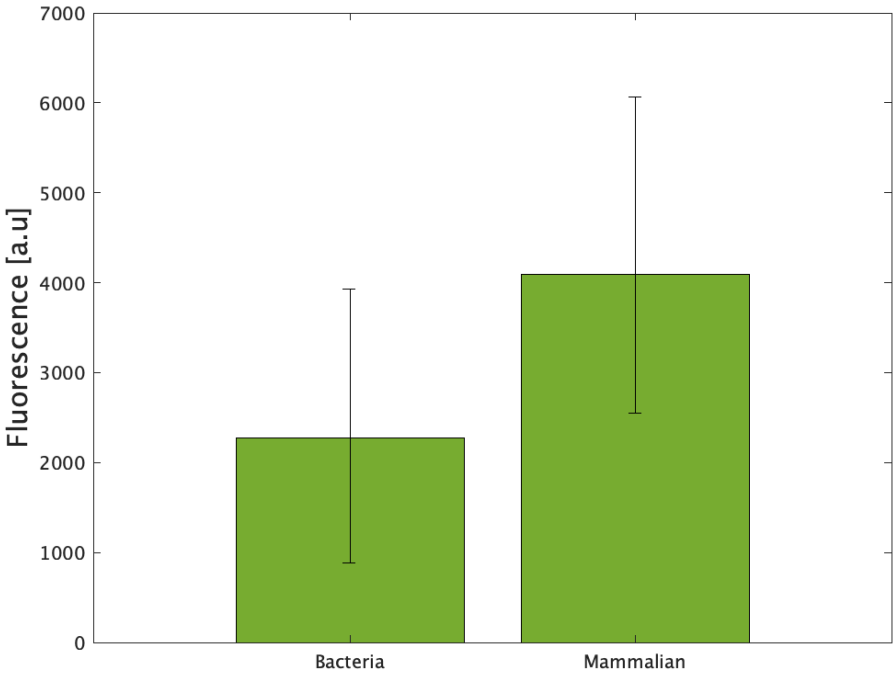

Figure 3.8: Measured fluorescent of bacterial- and mammalian liposome mixtures after treatment with GO-F

3.2.4 Heat capacity of liposomes

Fig. 3.9 shows the outcome from the differential scanning calorimetry (DSC) measurements. Measurements carried out between 25-70 °C, thus, no major weight changes are expected. Therefore, we are only interested in the data from DSC measurement (excluded TGA). Also, the most significant happenings took place before 42°C, which is convenient, and we choose to highlight the results within the temperature range of 25-42 °C. Due to running out of the stock-solution of PS, liposomes with this phospholipid were not measured.

For bacterial liposomes, there are a wide spread of outcomes. No endothermic peaks are present at this temperature range for the 50/50% mixed phospholipid liposome (CL/PG). For 100% PG, the endothermic peak takes place at lower temperature (29.2 °C, 0.036 µV/mg), compared to the other liposomes, which indicates that the amount of heat needed to overcome the endothermic reaction is lower. The second lowest peak is exhibited for 100% CL (33.2 °C, 0.061 µV/mg), which also represents the bacterial membrane. The other liposomes have similar maximum peaks, with a slight shift in temperature dependency. The most temperature resistant liposome seems to be the one representing the cancer cells (100% PE), which exhibit an endothermic peak at 33.4 °C with a heat flow of 0.076 µV/mg.

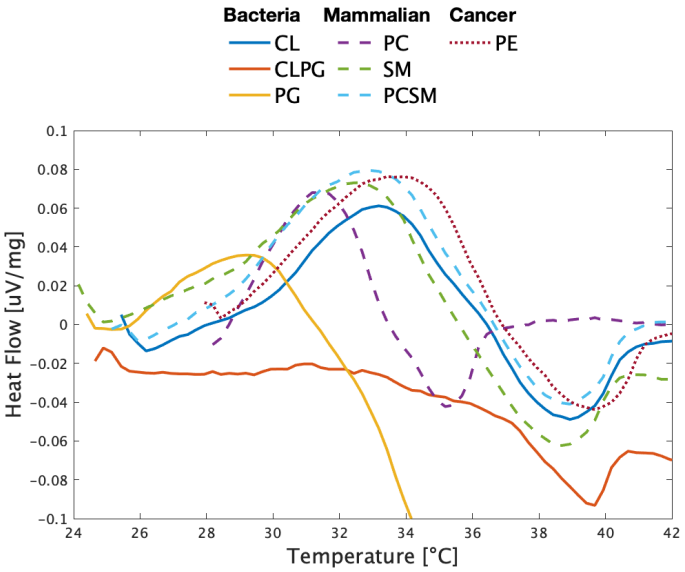

Figure 3.9: The DSC curves from measured liposomes between 25-42°C.

Calculating the integral for each endothermic peak, with respect to time (not temperature) we get the heat capacity, as µVs/mg. Table 3.1 presents the results from these calculations. For 50/50% CL/PG, endothermic peak was not present, and thus, the heat capacity from this liposome could not be calculated. And, as indicated from the DSC curves, the bacterial liposomes display lowest heat capacity, and the cancer liposomes the highest.

Table 3.1: Table of the measured heat capacity of liposomes

Organisms	Phospholipid	Heat capacity [uVs/mg]
Bacteria	CL	0.176
	PG	0.093
	CL/PG	-
Mammalian	PC	0.229
	SM	0.301
	PC/SM	0.279
Cancer	PE	0.333
	PS	-
	PE/PS	-

Next, the values from the calculated heat capacities were converted from µVs/mg to µVs/mol, and plotted against the theoretical calculations. Since no calibration was done before the DSC measurement, the units could not be converted into J/mols, as the theoretical. Nevertheless, if we fit the measured heat capacities into the theoretical plot, we see that they follow the same pattern and range. This strengthen the theoretical predictions of weaker interaction between the bacterial phospholipids compared to both mammalian and cancer phospholipids. However, since the solution of PS run out of stock, only one liposome mix was measured the cancer membranes. Also, all liposomes were assembled in H_2O:EtOH solution, without removing EtOH, which also need to be considered.

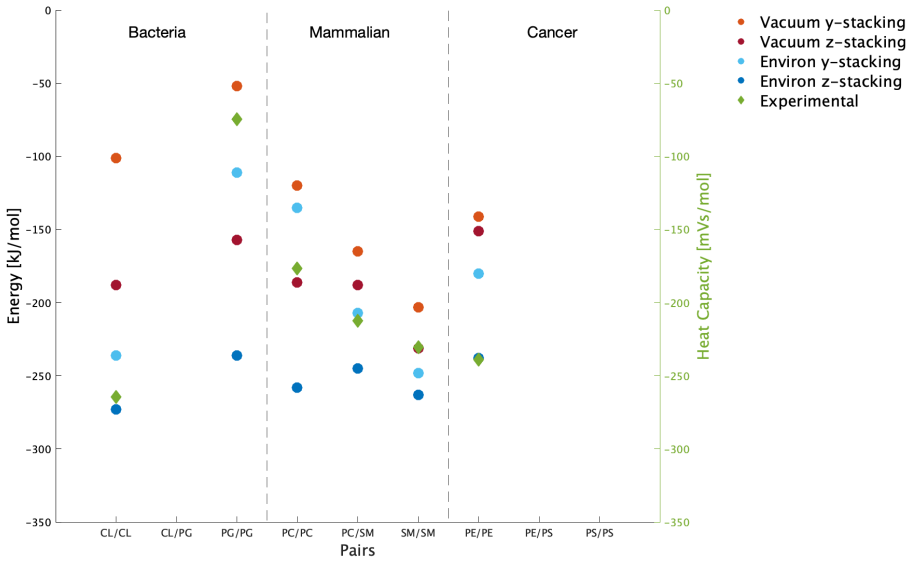
Bacteria
Mammalian
Cancer
Energy [kJ/mol]
Heat Capacity [mVs/mol]
Pairs
CL/CL
CL/PG
PG/PG
PC/PC
PC/SM
SM/SM
PE/PE
PE/PS
PS/PS
Vacuum y-stacking
Vacuum z-stacking
Environ y-stacking
Environ z-stacking
Experimental

Figure 3.10

4

Conclusion and perspectives

4.1 Analysis of result

From the results, we can conclude that functionalization of graphene oxide with fluorescein is possible, and that the fluorescent property is dependent on solvent and specifically, the pH level. It can also be stated that when assemble liposomes, concentration of phospholipid and ratio between H_2O:EtOH affects the sizes of liposomes. Higher phospholipid concentration and lower H_2O:EtOH ratio leads to larger liposomes.

Further, internalization of GO-F into liposomes was visualized with fluorescent microscope. This indicated more internalization of GO-F into mammalian- and cancer liposomes compared to that of bacterial ones. In quantitative analysis higher fluorescent signal was found for the mammalian liposomes, after treating selected bacterial and mammalian liposomes with GO-F. This could be connected to the theoretical calculations which showed that bacterial phospholipids exhibit less repulsive forces to approaching GO-flake, and thus, higher possibility for cutting and disrupting the membrane. The mammalian phospholipids display higher repulsive forces to approaching GO-flake in the theoretical calculations, which can restrict membrane penetration, while enabling internalization instead.

Next, when analyzing the DSC measurements of the liposomes, a distinct shift in heat resistant were found for the bacterial liposomes compared to the mammalian- and cancer liposomes. The endothermic reactions took place at lower temperatures and/or with a lower maximum peak for the bacterial liposomes. Also, the bacterial liposomes exhibited lower heat capacity which goes in line with the theoretical calculations, which was visualized in fig.3.10. One explanation could be that the bacterial phospholipids contains more OH-groups in their heads, which creates a ”special” arrangement with higher numbers of intramolecular forces, and less intermolecular attractions between the phospholipids. Also, the results from the theoretical part shows that z-stacking leads to higher numbers of possible interactions, and thus, stronger bonding between the phospholipids. Adding the environ plug-in into the calculations leads to a decrease in energy for all the systems. This could be interpreted by the hydrophobic/hydrophilic properties, where water pushes the hydrophobic tails closer to each other, which allows for more interactions. Also, the environ plug-in, together with z-stacking seems to ”even out” the energies between the systems and the contribution from the head groups becomes less significant.

4.2 Outlook

The calculations for the approaching flakes were performed with SCF calculations, and no movement of ions are allowed. Thus, implementing relaxed state calculations and/or molecular dynamics would be closer to reality. Also, the SCF-calculations did not include environ plug-in, which could change the outcome. For the practical part, quantification of liposomes survival after GO-F treatment can be done to validate cutting membrane by GO-flakes. This could strengthen the theoretical calculations and further confirm the cause of lower fluorescent signal after treatment of bacterial liposomes with the functionalized fluorescein GO. Also, ethanol was not extracted from the liposome solutions after synthesise, which could effect the solubility of liposomes and their characteristics.

Bibliography

[1] Santosh Pandit et al. "Vertically Aligned Graphene Coating is Bactericidal and Prevents the Formation of Bacterial Biofilms". In: *Advanced Materials Interfaces* 5.7 (2018), p. 1701331. DOI: https://doi.org/10.1002/admi.201701331.

[2] Jorge Bernardino de la Serna et al. "There Is No Simple Model of the Plasma Membrane Organization". In: *Frontiers in Cell and Developmental Biology* 4 (2016). DOI: 10.3389/fcell.2016.00106.

[3] M. Aldeghi and P.C. Biggin. "3.02 - Advances in Molecular Simulation". In: *Comprehensive Medicinal Chemistry III*. Ed. by Samuel Chackalamannil, David Rotella, and Simon E. Ward. Oxford: Elsevier, 2017, pp. 14–33. ISBN: 978-0-12-803201-5. DOI: https://doi.org/10.1016/B978-0-12-409547-2.12343-1.

[4] David J. Huggins et al. "Biomolecular simulations: From dynamics and mechanisms to computational assays of biological activity". In: *WIREs Computational Molecular Science* 9.3 (2019), e1393. DOI: https://doi.org/10.1002/wcms.1393.

[5] K. S. Novoselov et al. "Two-dimensional atomic crystals". In: *Proceedings of the National Academy of Sciences* 102.30 (2005), pp. 10451–10453. DOI: https://10.1073/pnas.0502848102.

[6] Graphene Flagship. *The Graphene Flagship*. 2013. URL: https://graphene-flagship.eu/collaboration/about-us/the-graphene-flagship/. (accessed: 28.01.2022).

[7] Ke Cao et al. "Elastic straining of free-standing monolayer graphene". In: *Nature Communications* 11.284 (2020). DOI: https://doi.org/10.1038/s41467-019-14130-0.

[8] Yan Wang et al. "Graphene-based nanomaterials for cancer therapy and anti-infections". In: *Bioactive Materials* 14 (2022), pp. 335–349. DOI: https://doi.org/10.1016/j.bioactmat.2022.01.045.

[9] Yanyan Chen et al. "Interactions Between Graphene-Based Materials and Biological Surfaces: A Review of Underlying Molecular Mechanisms". In: *Advanced Materials Interfaces* 8.24 (2021), p. 2101132. DOI: https://doi.org/10.1002/admi.202101132.

[10] Phospholipid Research Center. *The unique and different types of phospholipids*. URL: https://www.phospholipid-research-center.com/phospholipid/types/. (accessed: 14.04.2022).

[11] Phospholipid Research Center. *The various phospolipid aggregates*. URL: https://www.phospholipid-research-center.com/phospholipid/aggregates/. (accessed: 14.04.2022).

[12] Evelyne Deplazes et al. "The effect of H3O+ on the membrane morphology and hydrogen bonding of a phospholipid bilayer". In: *Biophysical reviews* 10 (2018), pp. 1371–1378. DOI: https://doi.org/10.1007/s12551-018-0454-z.

[13] Wolfram Koch and Max C. Holthausen. *A chemist's guide to density functional theory*. Wiley-VCH, 2001. ISBN: 3527304223. URL: https://search.ebscohost.com/login.aspx?direct=true&db=cat07470a&AN=clc.ba9924b5.5005.4786.a2d7.630166a46a58&site=eds-live&scope=site&authtype=guest&custid=s3911979&groupid=main&profile=eds.

[14] David S. Sholl and Janice A. Steckel. *Density functional theory : a practical introduction*. Wiley, 2009. ISBN: 9780470373170. URL: https://search.ebscohost.com/login.aspx?direct=true&db=cat07470a&AN=clc.98516e9a.ab0b.4a0e.9956.4148ca64567e&site=eds-live&scope=site&authtype=guest&custid=s3911979&groupid=main&profile=eds.

[15] E. Schrödinger. "An Undulatory Theory of the Mechanics of Atoms and Molecules". In: *Phys. Rev.* 28 (6 Dec. 1926), pp. 1049–1070. DOI: 10.1103/PhysRev.28.1049. URL: https://link.aps.org/doi/10.1103/PhysRev.28.1049.

[16] P. Hohenberg and W. Kohn. "Inhomogeneous Electron Gas". In: *Phys. Rev.* 136 (3B Nov. 1964), B864–B871. DOI: 10.1103/PhysRev.136.B864. URL: https://link.aps.org/doi/10.1103/PhysRev.136.B864.

[17] W. Kohn and L. J. Sham. "Self-Consistent Equations Including Exchange and Correlation Effects". In: *Phys. Rev.* 140 (4A Nov. 1965), A1133–A1138. DOI: 10.1103/PhysRev.140.A1133. URL: https://link.aps.org/doi/10.1103/PhysRev.140.A1133.

[18] NobelPrize.org. *The Nobel Prize in Chemistry 1998.* URL: https://www.nobelprize.org/prizes/chemistry/1998/summary/. (accessed: 03.04.2022).

[19] Quantum ESPRESSO. *manifesto.* May 2021. URL: https://www.quantum-espresso.org/manifesto/.

[20] Paolo Giannozzi et al. "QUANTUM ESPRESSO: a modular and open-source software project for quantum simulations of materials". In: *Journal of Physics: Condensed Matter* 21.39 (Sept. 2009), p. 395502. DOI: 10.1088/0953-8984/21/39/395502.

[21] P Giannozzi et al. "Advanced capabilities for materials modelling with Quantum ESPRESSO". In: *Journal of Physics: Condensed Matter* 29.46 (Oct. 2017), p. 465901. DOI: 10.1088/1361-648x/aa8f79.

[22] Paolo Giannozzi et al. "Quantum ESPRESSO toward the exascale". In: *The Journal of Chemical Physics* 152.15 (2020), p. 154105. DOI: 10.1063/5.0005082.

[23] Kevin F. Garrity et al. "Pseudopotentials for high-throughput DFT calculations". In: *Computational Materials Science* 81 (2014), pp. 446–452. ISSN: 0927-0256. DOI: https://doi.org/10.1016/j.commatsci.2013.08.053.

[24] T. Thonhauser et al. "Spin Signature of Nonlocal Correlation Binding in Metal-Organic Frameworks". In: *Phys. Rev. Lett.* 115 (13 Sept. 2015), p. 136402. DOI: 10.1103/PhysRevLett.115.136402.

[25] T. Thonhauser et al. "Van der Waals density functional: Self-consistent potential and the nature of the van der Waals bond". In: *Phys. Rev. B* 76 (12 Sept. 2007), p. 125112. DOI: 10.1103/PhysRevB.76.125112.

[26] Kristian Berland et al. "van der Waals forces in density functional theory: a review of the vdW-DF method". In: *Reports on Progress in Physics* 78.6 (May 2015), p. 066501. DOI: 10.1088/0034-4885/78/6/066501.

[27] D C Langreth et al. "A density functional for sparse matter". In: *Journal of Physics: Condensed Matter* 21.8 (Jan. 2009), p. 084203. DOI: 10.1088/0953-8984/21/8/084203.

[28] Hendrik J. Monkhorst and James D. Pack. "Special points for Brillouin-zone integrations". In: *Phys. Rev. B* 13 (12 June 1976), pp. 5188–5192. DOI: 10.1103/PhysRevB.13.5188.

[29] National Library of Medicine. *PubChem.* URL: https://pubchem.ncbi.nlm.nih.gov/. (accessed: 05.04.2022).

[30] Anton Kokalj. "Computer graphics and graphical user interfaces as tools in simulations of matter at the atomic scale". In: *Computational Materials Science* 28.2 (2003), pp. 155–168. ISSN: 0927-0256. DOI: https://doi.org/10.1016/S0927-0256(03)00104-6.

[31] Amedeo Bellunato et al. "Chemistry at the Edge of Graphene". In: *ChemPhysChem* 17.6 (2016), pp. 785–801. DOI: https://doi.org/10.1002/cphc.201500926.

[32] Daniel R. Dreyer et al. "The chemistry of graphene oxide". In: *Chem. Soc. Rev.* 39 (1 2010), pp. 228–240. DOI: 10.1039/B917103G.

[33] GRAPHENE SUPERMARKET. *Ultra Highly Concentrated Single-Layer Graphene Oxide.* URL: https://www.graphene-supermarket.com/products/copy-of-ultra-highly-concentrated-single-layer-graphene-oxide-60-ml?pr_prod_strat=collection_fallback&pr_rec_pid=6931503055057&pr_ref_pid=6931500826833&pr_seq=uniform.

[34] Heyong He et al. "Solid-State NMR Studies of the Structure of Graphite Oxide". In: *The Journal of Physical Chemistry* 100.51 (1996), pp. 19954–19958. DOI: 10.1021/jp961563t.

[35] Christian Sohlenkamp and Otto Geiger. "Bacterial membrane lipids: diversity in structures and pathways". In: *FEMS Microbiology Reviews* 40.1 (Apr. 2015), pp. 133–159. ISSN: 0168-6445. DOI: 10.1093/femsre/fuv008.

[36] Shin-ya Morita, Tokuji Tsuji, and Tomohiro Terada. "Protocols for Enzymatic Fluorometric Assays to Quantify Phospholipid Classes". In: *International Journal of Molecular Sciences* 21.3 (2020). ISSN: 1422-0067. DOI: 10.3390/ijms21031032.

[37] Giulio Preta. "New Insights Into Targeting Membrane Lipids for Cancer Therapy". In: *Frontiers in Cell and Developmental Biology* 8 (2020). ISSN: 2296-634X. DOI: 10.3389/fcell.2020.571237.

[38] Giulio Preta. "New Insights Into Targeting Membrane Lipids for Cancer Therapy". In: *Frontiers in Cell and Developmental Biology* 8 (2020). DOI: 10.3389/fcell.2020.571237.

[39] Cheng Peng et al. "Intracellular Imaging with a Graphene-Based Fluorescent Probe". In: *Small* 6.15 (2010), pp. 1686–1692. DOI: https://doi.org/10.1002/smll.201000560.

[40] Christy R. Cuthbertson and Melissa A. Parsey. “An Introduction to Lipid Nanoparticle Formulation: Basic Concepts Preparation Procedures”. In: (2022). URL: https://www.caymanchem.com/news/intro-to-lipid-nanoparticle-formulation. (accessed: 07.12.2022).

[41] Kira L. F. Hilton et al. “The phospholipid membrane compositions of bacterial cells, cancer cell lines and biological samples from cancer patients”. In: *Chem. Sci.* 12 (40 2021), pp. 13273–13282. DOI: 10.1039/D1SC03597E.

[42] J. A. Virtanen, K. H. Cheng, and P. Somerharju. “Phospholipid composition of the mammalian red cell membrane can be rationalized by a superlattice model”. In: *Proceedings of the National Academy of Sciences* 95.9 (1998), pp. 4964–4969. DOI: 10.1073/pnas.95.9.4964.

[43] Joseph Jose, Hemalatha Kanniyappan, and Vignesh Muthuvijayan. “A novel, rapid and cost-effective method for separating drug-loaded liposomes prepared from egg yolk phospholipids”. In: *Process Biochemistry* 115 (2022), pp. 80–91. ISSN: 1359-5113. DOI: https://doi.org/10.1016/j.procbio.2022.02.010.

[44] SIGMA. “Productinformation: Fluorescein”. In: (). URL: https://www.sigmaaldrich.com/deepweb/assets/sigmaaldrich/product/documents/235/357/f7505pis.pdf. (accessed: 09.12.2022).

[45] Arne S. Kristoffersen et al. “Testing Fluorescence Lifetime Standards using Two-Photon Excitation and Time-Domain Instrumentation: Fluorescein, Quinine Sulfate and Green Fluorescent Protein”. In: *Journal of Fluorescence volume* 28 (2018), pp. 1065–1073. DOI: doi.org/10.1007/s10895-018-2270-z.

[46] M. Born and R. Oppenheimer. “Zur Quantentheorie der Molekeln”. In: *Annalen der Physik* 389.20 (1927), pp. 457–484. DOI: https://doi.org/10.1002/andp.19273892002. eprint: https://onlinelibrary.wiley.com/doi/pdf/10.1002/andp.19273892002. URL: https://onlinelibrary.wiley.com/doi/abs/10.1002/andp.19273892002.

[47] V. Fock. “„Selfconsistent field“ mit Austausch für Natrium”. In: *Zeitschrift für Physik* 60 (1930), pp. 795–805. DOI: https://doi.org/10.1007/BF01330439.

[48] Douglas Rayner Hartree and W. Hartree. “Self-consistent field, with exchange, for beryllium”. In: *Proceedings of the Royal Society of London. Series A - Mathematical and Physical Sciences* 150.869 (1935), pp. 9–33. DOI: 10.1098/rspa.1935.0085. URL: https://royalsocietypublishing.org/doi/abs/10.1098/rspa.1935.0085.

[49] J. C. Slater. “The Theory of Complex Spectra”. In: *Phys. Rev.* 34 (10 Nov. 1929), pp. 1293–1322. DOI: 10.1103/PhysRev.34.1293. URL: https://link.aps.org/doi/10.1103/PhysRev.34.1293.

[50] L. H. Thomas. “The calculation of atomic fields”. In: *Mathematical Proceedings of the Cambridge Philosophical Society* 23.5 (1927), pp. 542–548. DOI: 10.1017/S0305004100011683.

[51] O. Gunnarsson and B. I. Lundqvist. “Exchange and correlation in atoms, molecules, and solids by the spin-density-functional formalism”. In: *Phys. Rev. B* 13 (10 May 1976), pp. 4274–4298. DOI: 10.1103/PhysRevB.13.4274. URL: https://link.aps.org/doi/10.1103/PhysRevB.13.4274.

[52] Kieron Burke, John P. Perdew, and Matthias Ernzerhof. “Why the generalized gradient approximation works and how to go beyond it”. In: *International Journal of Quantum Chemistry* 61.2 (1997), pp. 287–293. DOI: https://doi.org/10.1002/(SICI)1097-461X(1997)61:2<287::AID-QUA11>3.0.CO;2-9.

[53] Elisa Londero. *Theory of van der Waals bonding : from bulk materials to biomolecules.* Technical report MC2: 238. Department of Microtechnology and Nanoscience (MC2), Chalmers University of Technology, 2012. ISBN: 9789173857864. URL: https://search.ebscohost.com/login.aspx?direct=true&db=cat07470a&AN=clc.72ddd125.e2a7.4fdb.b541.24b52c00b022&site=eds-live&scope=site&authtype=guest&custid=s3911979&groupid=main&profile=eds.

[54] *vdW-DF activities.* URL: http://fy.chalmers.se/~schroder/vdWDF/. (accessed: 03.04.2022).

[55] M. Dion et al. “Van der Waals Density Functional for General Geometries”. In: *Phys. Rev. Lett.* 92 (24 June 2004), p. 246401. DOI: 10.1103/PhysRevLett.92.246401. URL: https://link.aps.org/doi/10.1103/PhysRevLett.92.246401.

A

Appendix I

The route from Schrödinger equations to density functional theory

Density functional theory (DFT) is equivalent to the fundamental equation of quantum mechanical systems, the Schrödinger equation (SE)[13][14]. In 1926, Erwin Schrödinger published a series of papers where he postulated "that material points consist of, or are nothing but, wave-systems" and derived this into the mathematical equation

$$\hat{H}\Psi = i\hbar\frac{\delta}{\delta t}\Psi \tag{A1}$$

which is also called the time-dependent SE [15]. A simplified form for time invariant potentials, is the time-independent, non-relativistic SE

$$\hat{H}\Psi = E\Psi \tag{A2}$$

where $\hat{H}$ is the Hamilton operator for the system and Ψ is the wave function to a set of eigenstates of the Hamiltonian with the associated eigenvalue E. With variational methods, the solution for the lowest eigenvalue of a stationary state can in principle be found, hence the ground state. Schrödinger set by these expressions the foundation for the future theory of quantum mechanical systems. Both the time-dependent and the time-independent SE are what many scientist in the quantum field have been trying to solve over the years, but exact solutions are not possible for more than a few particles. Therefore, many approaches to these equations have been evolved and one of these is the DFT, which is exact as the time-independent SE, but to solve it for practical purposes, approximations are used. In eq.(A2), the Hamiltonian is used and the time-independent SE can be expressed as

$$\Big[-\frac{\hbar}{2m_i}\sum_{i=1}^{N}\nabla_i^2 - \frac{\hbar}{2m_a}\sum_{a=1}^{M}\nabla_a^2 + \sum_{i=1}^{N}\sum_{a=1}^{N}V(r_i,r_a) + \sum_{i=1}^{N}\sum_{j>1}^{N}U(r_i,r_j) + \sum_{a=1}^{N}\sum_{b>1}^{N}U(r_a,r_b)\Big]\Psi = E\Psi \tag{A3}$$

with the two first expressions being the kinetic energy for the electrons (i) and nuclei (a). The three last terms are the potential energy of the system and represent the attractive electrostatic interaction between electron(i)-nuclei(a) and the repulsive potential between electron(i)-electron(j) and nuclei(a)-nuclei(b). SE has been solved exactly for a single-particle system where models like particle in a box and harmonic oscillator have been used to describe these problems. For a many-body system where multiple particles are interacting the SE becomes more complicated which makes exact analytical calculations impossible. Several models have been developed during the years to deal with this problem, and until now, all models rely on approximations of various kinds.

One improvement is to realize that the atoms and electrons move on very different timescales, due to the mass differences (the mass of the electron is at least a factor 2000 smaller than the atom). In 1927, this was recognized by Max Born and J. Robert Oppenheimer [46], who proposed the Born-Oppenheimer approximation. The consequence is that the system can be approximated by considering the electron moving in the field of fixed nuclei. This means, roughly speaking, that the kinetic energy from the nuclei is zero and the nuclei-nuclei repulsion is a constant. The Hamiltonian can therefore be split and reduced to

$$\hat{H} = -\frac{\hbar}{2m_i}\sum_{i=1}^{N}\nabla_i^2 + \sum_{i=1}^{N}V(r_i) + \sum_{i=1}^{N}\sum_{j>1}^{N}U(r_i,r_j) \tag{A4}$$

Further approximation to the many-body system was done by Douglas Rayner Hartree and Vladimir Aleksan-

drovich Fock [47][48] by simplifying the wave function into a Slater determinant [49]

$$\Psi_{SD} = \frac{1}{\sqrt{N!}} det \begin{bmatrix} \chi_1(\vec{x_1}) & \chi_2(\vec{x_1}) & ... & \chi_N(\vec{x_1}) \\ \chi_1(\vec{x_2}) & \chi_2(\vec{x_2}) & ... & \chi_N(\vec{x_2}) \\ . & . & . & . \\ . & . & . & . \\ . & . & . & . \\ \chi_1(\vec{x_N}) & \chi_2(\vec{x_N}) & ... & \chi_N(\vec{x_N}) \end{bmatrix} \tag{A5}$$

where $\chi_1(\vec{x_1})$ denotes the spin orbitals and are composed of two spin functions, up or down, and a spatial orbital. They expressed the so called Hartree-Fock (HF) approximation as

$$\hat{H}_{HF}\Psi_{SD} = E_{HF}\Psi_{SD} \tag{A6}$$

The Hamiltonian in the HF approximation still contains the contribution from the kinetic energy, the electron-nuclei attraction and the electron-electron repulsion. The electrostatic electron-electron interaction was expressed as an average repulsive potential each electron experiences from its surrounding electrons, also called the HF potential (V_{HF}), and expressed as

$$V_{HF} = \sum_{j}^{N} (\hat{J}_j(\vec{x_1}) - \hat{K}_j(\vec{x_1})) \tag{A7}$$

The HF potential includes $\hat{J}_j$ and represents the Coulomb operator, the electron-electron repulsion from the j-th orbital. The $\hat{K}_j$ is the exchange operator and describes the electron exchange energy due to the antisymmetry of the N-electron wave function. They also took advantage of the variational principle to find the optimal wave function (Ψ_0). This principle states that if any trial wave function (Ψ_{tri}) is chosen and computed together with the Hamilton operator of the SE, the expectation value of that eigenvalue (E_{trial}) must be equal to, or higher than the true energy. Therefore, E_{trial} is used as an upper bound to the ground state energy levels and written with Dirac notations as

$$\langle \Psi_{trial}|\hat{H}|\Psi_{trial}\rangle = E_{trial} \geq E_0 = \langle \Psi_0|\hat{H}|\Psi_0\rangle \tag{A8}$$

This was the birth of the self-consistent field, which is an iterative method that computes the wave-function until it converges with the true SE. Unfortunately, the HF approach is only feasible for small systems and becomes computational expensive with increased numbers of particles [13].

During the same time period, 1927, another approximation method was published, the Thomas-Fermi model [50]. Llewellyn Thomas and Enrico Fermi describe the system as a uniform electron gas where they use a statistical model to predict the behavior of a many-body system by calculating the electronic density rather than the wave function. The importance of this equation is however not in the yield of quantitative predictions, but it should be highlighted that this was the first model where the energy is expressed only in terms of the electron density. Because of its inaccuracy, the TF model did not receive too much of attention and it was not until 1964 when Pierre Hohenberg and Walter Kohn developed this further with their two Hohenberg-Kohn (HK) theorems [16], and then one year later expanded by Walter Kohn and Lu Jeu Sham into the Kohn-Sham (KS) theorem [17]. These theorems were the birth of DFT and Walter Kohn was awarded the Nobel Prize in chemistry 1998 for his contributions to computational chemistry [18].

The first HK theorem proved that the ground state energy from SE is a unique functional of the electron density $n(\vec{r})$

$$n(\vec{r}) = 2\sum_{i} \psi_i^*(\vec{r})\psi_i(\vec{r}) \tag{A9}$$

They first denoted the electron density in the ground state as a functional of the external potential $V(\vec{r})$, and then by reductio ad absurdum, they proved that $n(\vec{r})$ is a unique functional of $\vec{r}$. Since the energy is dependent on $\vec{r}$, they stated that the ground state for a full many-particle system should also be a unique function of $\vec{r}$. They defined the energy functional as

$$E[n(\vec{r})] = \int V(\vec{r})n(\vec{r})d^3r + F[n(\vec{r})] \tag{A10}$$

with

$$F[n(\vec{r})] = \langle \psi|T + U|\psi\rangle \tag{A11}$$

where T is the kinetic energy and U the Coulomb electron-electron interactions. This functional was further transformed into the form

$$F[n(\vec{r})] = \frac{1}{2}\int \frac{n(\vec{r})n(\vec{r'})}{|r - r'|} d^3r d^3r' + G[n(\vec{r})] \tag{A12}$$

with $G[n(\vec{r})]$ as a universal functional of the density.

The second HK theorem defined an important property for the functional. The input for the true ground state density should deliver the lowest energy and thus the ground state of the system. They took advantage of the variational principle and expressed that any trial electron density $n(\vec{r})_{trial}$ is the upper bound for the true ground state as

$$\langle \Psi_{trial}|\hat{H}|\Psi_{trial}\rangle = \int V(\vec{r})n(\vec{r})_{trial}d^3r + F[n(\vec{r})_{trial}] = E[n(\vec{r})_{trial}] \geq E_0[n(\vec{r})_0] = \langle \Psi_0|\hat{H}|\Psi_0\rangle \tag{A13}$$

If the true functional were known, then the electron density could be varied until the energy from the functional is minimized and thus solve the relevant electron density. For this to be true it is necessary that minimized energy does not change the number of electrons. They used the Lagrange multiplier and expressed the condition as

$$\delta E[n(\vec{r})] - \mu \int n(\vec{r})d^3r = 0 \tag{A14}$$

with μ as a Lagrange parameter. This was then rearranged into

$$\delta \frac{F[n(\vec{r})]}{\delta n} + V(\vec{r}) = \mu \tag{A15}$$

Until this point, the computational effort was reduced from 3N variables of the wave function into three spatial variables for the electron density, but they did not say what the functional actually was and solving the SE was thus still an issue. Kohn and Sham suggested how this could be approached and developed the KS equations. They introduced the concept of a single-electron wave functions. They started by assuming that there was no contribution from the electron-electron interactions and reduced the universal functional to

$$F[n(\vec{r})] = T[n(\vec{r})] \tag{A16}$$

which is only dependent of the kinetic energy. In this way, the contribution from the kinetic energy was solved with a much higher accuracy than the former Thomas-Fermi equations. The kinetic energy was formulated as

$$T[n(\vec{r})] = \sum \int d^3r\psi_i^*(\vec{r}) \left(-\frac{\hbar}{2m_i} \sum_{i=1}^{N} \nabla_i^2 \right) \psi_i(\vec{r}) \tag{A17}$$

Since this is the kinetic energy from a non-interacting system, they could not say that this is equal to the true kinetic energy for a interacting system. Kohn and Sham added some terms for an interacting system and expressed it as

$$F[n(\vec{r})] = T[n(\vec{r})] + U[n(\vec{r})] + E_{xc}[n(\vec{r})] \tag{A18}$$

with $U[n(r)]$ as the Coulombic electron-electron interaction

$$U[n(\vec{r})] = \frac{1}{2} \int \int d^3r d^3r' \frac{n(\vec{r})n(\vec{r}')}{r - r'} \tag{A19}$$

and $E_{xc}[n(r)]$ as the exchange-correlation energy. This expression is solved approximately and contains everything unknown from the kinetic energy of a interacting system together with the potential energy from self-interacting effects. The equation to be minimized is now

$$E[n(\vec{r})] = T[n(\vec{r})] + V[n(\vec{r})] + U[n(\vec{r})] + E_{xc}[n(\vec{r})] \tag{A20}$$

and from the constraints of the Lagrange multiplier

$$\delta E[n(\vec{r})] - \sum \epsilon_i \int d^3r\psi^*(\vec{r})n(\vec{r})\psi(\vec{r}) = 0 \tag{A21}$$

with ϵ_i as the i-th Lagrange parameter, the KS equations were reduced to a one-particle SE and took the form

$$\left[-\frac{\hbar^2}{2m} \nabla^2 + V_{KS}(\vec{r}) \right] \psi_i(\vec{r}) = \epsilon_i \psi_i(\vec{r}) \tag{A22}$$

with the KS potential as

$$V_{KS}(\vec{r}) = V(\vec{r}) + U(\vec{r}) + E(\vec{r}) = \int V(\vec{r})n(\vec{r})d^3r + e^2 \int \frac{n(\vec{r}')}{|r - r'|} d^3r' + \frac{\delta E_{xc}[n(\vec{r})]}{\delta n(\vec{r})} \tag{A23}$$

Exchange-correlation functionals

In the KS equation the form of the exchange-correlation functional is unknown and is therefore treated in a approximate manner. A number of methods to define these functionals have been developed. The first approach was proposed by Kohn and Sham and is called the local density approximation (LDA) [17]. This assumes that the system consists of a uniform electron gas where the electron density is constant at all points in space

$$E_{xc}^{LDA}[n] = \int n(\vec{r})\epsilon_{xc}(n(\vec{r}))d^3r \tag{A24}$$

with $\epsilon_{xc}(n(\vec{r}))$ as the exchange-correlation energy per particle in a homogeneous electron gas with density $n(\vec{r})$. This was further developed, by considering the spins of the electrons, into the local spin density approximation (LSDA) [51]

$$E_{xc}^{LSDA}[n_\uparrow, n_\downarrow] = \int n(\vec{r})\epsilon_{xc}(n_\uparrow, n_\downarrow)d^3r \tag{A25}$$

Another approach is the generalized gradient approximation (GGA) [52]

$$E_{xc}^{GGA}[n_\uparrow, n_\downarrow] = \int n(\vec{r})\epsilon_{xc}(n_\uparrow, n_\downarrow, \nabla n_\uparrow, \nabla n_\downarrow)d^3r \tag{A26}$$

This uses information from the LSDA together with a local gradient in the electron density. How this gradient is included in the equation could also vary and different GGA functionals therefore exist. Two of the most widely used is the Perdew-Wang functional (PW91) and the Perdew-Burke-Ernzerhof functional (PBE) [14]. Since this method accounts for the gradient of the density, it has become widely used for solid state calculations which often comprises of smaller distances such as covalent, ionic and metal bonds. However, with longer distances between particles, fluctuations of charges located far away from each other could cause van-der-Waals (vdW) interactions and these forces are not considered in GGA functionals [53]. The GGA approach is therefore a good method to describe solid-state system but becomes less accurate in soft matter structures, where many biological molecules are included. The Rutgers-Chalmers collaboration [54] has developed the so called van der Waals density functional (vdW-DF) which extends to nonlocal, long-ranged interactions without loosing information from the local and semi-local functionals. It involved a numbers of papers and 2004, the description of vdW-DF for general geometries was published [55]. The starting point was to divide the exchange-correlation energy into

$$E_{xc}[n] = E_x[n] + E_c[n] \tag{A27}$$

where $E_x[n]$ is the contribution from the exchange term and $E_c[n]$ is the correlation energy. Both of these terms include nonlocal interactions, and the correlation term was further divided into

$$E_c[n] = E_c^0 + E_c^{nl} \tag{A28}$$

where E_c^{nl} describes the long-range, nonlocal interactions and E_c^0 is approximated with LDA. E_c^{nl} was derived to

$$E_c^{nl} = \frac{1}{2}\int d^3r d^3r' n(\vec{r})\phi(\vec{r},\vec{r}')n(\vec{r}') \tag{A29}$$

with $\phi(\vec{r},\vec{r}')$ as a general (kernel) function depending on the distance between $|r-r'|$ and the densities n close to $\vec{r}$ and $\vec{r}'$.

The kernel of van der Waals density functional

From Eq. A29, $\phi(\vec{r},\vec{r}')$ was expressed as a general (kernel) function depending on the distance between $|r-r'|$ and the densities n close to $\vec{r}$ and $\vec{r}'$. The kernel is further expressed as

$$\phi(\vec{r},\vec{r}') = \frac{2me^4}{\pi^2}\int_0^\infty a^2 da \int_0^\infty b^2 db W(a,b)T(\nu(a),\nu(b),\nu'(a),\nu'(b)) \tag{A30}$$

where

$$T(w,x,y,z) = \frac{1}{2}\left[\frac{1}{w+x}+\frac{1}{y+z}\right]\left[\frac{1}{(w+y)(x+z)}+\frac{1}{(w+z)(y+z)}\right] \tag{A31}$$

and

$$W(a,b) = 2\frac{(3-a^2)b\cos(b)\sin(a)+(3-b^2)a\cos(a)\sin(b)+(a^2+b^2-3)\sin(a)\sin(b)-3ab\cos(a)\cos(b)}{a^3b^3} \tag{A32}$$

ν and ν' are given as

$$\nu(y) = \frac{y^2}{2h\,(y/d)} \tag{A33}$$

$$\nu'(y) = \frac{y^2}{2h\,(/d')} \tag{A34}$$

where

$$d = |r - r'|q_0(\vec{r}) \tag{A35}$$

$$d' = |r - r'|q_0(\vec{r}') \tag{A36}$$

$$h(y) = 1 - e^{\gamma y^2} \tag{A37}$$

and q_0 is given as

$$q_0(\vec{r}) = \frac{\epsilon_{xc}^0(\vec{r})}{\epsilon_x^{LDA}(\vec{r})} k_F(\vec{r}) \tag{A38}$$

where

$$\epsilon_x^{LDA} = \frac{-3e^2 k_F}{4\pi} \tag{A39}$$

and

$$k_F = (3\pi^2 n)^{\frac{1}{3}} \tag{A40}$$

ϵ_{xc}^0 is approximated by using a gradient correction to LDA

$$\epsilon_{xc}^0 = \epsilon_{xc}^{LDA} - \epsilon_x^{LDA} \left[\frac{Z_{ab}}{9} \left(\frac{\nabla n}{2k_F n} \right)^2 \right] \tag{A41}$$

where

$$Z_{ab} = -0.8491 \tag{A42}$$

is the contribution from the screened response which was obtained from a diagrammatic analysis. Thus, the kernel depends on $\vec{r}$ and $\vec{r}'$, which can tabulated through d and d'. The exchange term in eq.A27 lacks a unique description in the vdW-DF method, and therefore, this is defined through some physical requirements which needs to be met. Different models to describe this term exist and in this paper is the vdW-DF-cx used where cx stands for consistent exchange.

Department of Biology and Biological Engineering
CHALMERS UNIVERSITY OF TECHNOLOGY
Gothenburg, Sweden, 2022
www.chalmers.se

Department of Biology and Biological Engineering
CHALMERS UNIVERSITY OF TECHNOLOGY
Gothenburg, Sweden, 2023